Article

Synaptic loss pattern is constrained by brain connectome and modulated by phosphorylated tau in Alzheimer's disease

Ying Luan [1,2,15], Weiyi Wang[1,15], Qi Huang[1,15], Yan Wang[1], Jana Nussbaumer [3], Jie Wang[1], Anna Steward[4], Sebastian N. Roemer-Cassiano [4,5,6], Yihui Guan[1], Michael Ewers [4], Michael Schöll [7,8,9,10], Ruiqing Ni [3,11] ✉, Binyin Li[12] ✉, Nicolai Franzmeier [4,8,13] & Fang Xie [1,14] ✉

Synaptic loss strongly correlates with cognitive impairment in Alzheimer's disease (AD), yet the mechanism linking its origin and pattern remain unclear. Given that connected brain regions share molecular and synaptic features, and pathological tau, a key driver of synaptic degeneration, propagates through brain networks, we hypothesize that network architecture may influence synaptic loss in AD. By combining synaptic vesicle glycoprotein 2 A (SV2A) PET in 91 AD patients and 54 controls with normative connectome data, we show strongly connected regions exhibit similar levels of synaptic loss, and synaptic loss in one region is associated with connectivity-weighted synaptic loss in connected regions. Regions strongly connected to the epicenter show greater and faster synaptic loss. Plasma p-tau181 levels correlate with network-constrained synaptic loss, and post-mortem data confirm reduced SV2A expression in tau-rich areas. These findings support that synaptic vulnerability in AD is partially constrained by network topology and is modulated by phosphorylated tau.

Alzheimer's disease (AD) is the most common neurodegenerative disease, which is characterized by the accumulation of extracellular amyloid-β (Aβ) plaques and intracellular tau neurofibrillary tangles (NFTs) in the brain. Synaptic dysfunction may lead to neurodegeneration and dementia[1] and is recognized as the strongest neurobiological correlates of cognitive impairment in AD[2]. Recent development

of PET ligands that binds synaptic vesicle glycoprotein 2 A (SV2A) has enabled in vivo visualization of synaptic density loss in AD as previously shown in post-mortem studies[3]. Emerging SV2A PET studies have consistently demonstrated a highly patterned distribution of synaptic loss in AD[4,5], suggesting that synaptic loss may propagate along specific pathways. However, the specific mechanisms linking

localized synaptic damages to patterned large-scale alterations throughout the brain in AD remain unclear.

Human brain is a highly structured network with complex connections, which facilitates the efficient interregional interactions and transport of molecules essential for metabolism and function[6,7]. This intrinsic topological architecture renders interconnected regions vulnerable to disease-related damage in a network-dependent manner[8]. Supporting this, brain areas within the same networks tend to exhibit shared gene expression profiles[9,10], morphological features[11], and maturational coupling[12], thus leading to a similar condition promoting pathological states. The concept of network-based selective vulnerability suggests that pathology propagates not only through direct pathological protein transmission but also through the shared susceptibility of interconnected regions[13]. Recent evidence shows that the synaptome network, constructed by a set of molecular and morphological features of synapses, closely resembles the functional network[14]. Additionally, connectivity-related gene expression profiles have been found to converge on synaptic signaling[15]. These findings indicate that interconnected regions exhibit similar synaptic properties and synapse-related gene expression, which may contribute to their vulnerability to disease-related synaptic loss. Moreover, in the context of AD, Aβ-induced synaptic damage triggers Ca²⁺ influx and mitochondrial dysfunction[16]. Due to the mobility of mitochondria in axons, ongoing Ca²⁺ influx leads to progressive mitochondrial damage that extends beyond the initial injury sites, spreading through the axonal connection and causing distal synaptic damage[17], as synaptic terminals have high energy demand[18]. Based on previous evidence, we speculate that the synaptic loss pattern in AD may be constrained by network architecture across interconnected regions, while this pattern has yet to be explicitly elucidated.

Aβ and tau are considered as the major contributors to synaptic loss in AD. Evidence implies that oligomeric Aβ induces excitotoxicity at the pre-synaptic terminal through interactions with various cell membrane receptors[19]. Detached pathological tau mislocates to synaptic compartments and induces toxicity to the synapses, particularly to synaptic vesicle proteins[20,21]. Inverse relationships between SV2A PET and amyloid[22] as well as tau PET[23–25] have been reported in hippocampus and medial temporal cortex, reinforcing the impact of AD pathologies on synaptic loss. A recent hypothesis[17] integrates previous evidence and proposes that at the early stage of AD, the synaptic damage caused by the initial deposition of Aβ can be efficiently cleared by microglia and restricted to local brain regions[26,27]. However, as Aβ load increases, axons interact with multiple plaques, resulting in the development of pathological tau at multiple sites. This ultimately leads to more severe and widespread synaptic loss rather than the localized loss surrounding individual plaques[28]. Furthermore, recent evidence has demonstrated that hyperphosphorylated tau (p-tau) leads to early synaptic damage preceding aggregated fibrillar tau[29,30]. Therefore, both Aβ and pathological tau may propagate synapse loss to distant brain regions[19]. However, direct evidence linking the Aβ and tau pathology to the distribution of synaptic loss remains lacking.

Recent advances in combining functional MRI and tau PET techniques have elucidated that AD pathology accumulation follows specific macroscale brain networks[31], suggesting that the pathology originates at the vulnerable core regions, and spread in a network-dependent manner. Specifically, interconnected regions share similar tau burden[32]. Aβ, tau, gray matter atrophy has been found to propagate following the specific connectivity profile[33–37]. Given the close link between AD pathology and synaptic degeneration, and in particular the ability of tau to propagate along functional networks and directly damage synapses, large-scale patterns of synaptic loss in AD may likewise be constrained by the brain's intrinsic network architecture in a similar manner as tau. Therefore, in the current study, we leveraged [18 F]SynVesT-1 SV2A-PET from 54 cognitively unimpaired amyloid-negative (CU Aβ−) controls and 91 amyloid-positive (Aβ+) participants, together with the normative brain connectome from 58 CU controls without Aβ or tau pathology to address the following open questions: (1) whether the pattern of synaptic loss is shaped by brain network connectome; (2) whether synaptic loss in AD distributes following the connectivity patterns to heterogeneous focal epicenters; and (3) whether the network-constrained distribution of synaptic loss is influenced by Aβ and p-tau.

Here we show a highly patterned spatial distribution of synaptic loss in AD, which is modestly constrained by the brain's network architecture. Despite inter-individual and subtype-level heterogeneity, the observed patterns of synaptic loss consistently follow the functional connectivity profiles to synaptic loss epicenters. Moreover, plasma p-tau levels significantly modulate the network-based distribution of synaptic degeneration. These findings provide a network-level perspective on synaptic vulnerability in AD and may advance future efforts to predict individual patterns of synaptic vulnerability based on network features.

Results
Sample characteristics
The basic demographics of the subjects across diagnostic groups (i.e., 54 CU Aβ−, 9 CU Aβ+, 28 MCI Aβ+, and 54 dementia Aβ+) are summarized in Table 1.

Group-average maps of the SV2A-PET standardized uptake value ratios (SUVRs) are shown in Fig. 1a. To quantify the change of synaptic density in Aβ+ participants, we adopted to a prior approach[38,39]. Briefly, we estimated a ROI-wise control GLM for SV2A-PET SUVR using CU Aβ- subjects, with age, sex, and cortical thickness as covariates. The SV2A-PET w-score for each subject was then calculated as the deviation of the actual ROI SV2A-PET SUVR from the predicted value based on the control model. This w score represents the standardized deviation of individual SV2A-PET SUVR relative to the CU Aβ-group, accounting for the effect of age, sex, and anatomical factor (see details in Methods and Materials). Group-average maps of the SV2A-PET w score illustrated a gradual decrease in SV2A-PET uptake across the AD spectrum compared to CU Aβ- group, particularly in the lateral temporal cortex, lateral frontal cortex, posterior cingulate cortex and precuneus (Fig. 1b, Supplementary Fig. 1). Among the Aβ+ participants, 18 participants underwent once follow-up of SV2A-PET scan. The annual change rate of SV2A-PET scores for each ROI were calculated as the difference of SV2A-PET w-score divided by the follow-up years (Fig. 1c).

Synaptic density loss covaries across connected brain regions
First, we tested our first hypothesis that interregional connectivity is associated with covarying synaptic loss between a given pair of brain regions. We determined the covariance in interregional SV2A-PET w scores in the CU Aβ- (Fig. 2a & e) and Aβ+ groups (Fig. 2b & f), and a functional connectivity template matrix (Fig. 2c & g) and a structural connectivity template matrix from 58 CU subjects without AD pathology (Fig. 2d & h). The demographics of the 58 CU subjects are show in Supplementary Table 1. The linear regression revealed expected association between stronger functional connectivity and greater covariance of SV2A-PET w scores was found in both the CU Aβ- (Fig. 2i, $\beta = 0.330$, $p_{rewired} < 0.001$) and Aβ+ groups (Fig. 2j, $\beta = 0.435$, $p_{rewired} < 0.001$), suggesting that functionally close regions show similar levels of synaptic loss. The distribution of β-values derived from 1000 bootstrapping resampling showed significantly stronger associations in Aβ+ participants (mean = 0.404; SD = 0.030) than in CU Aβ-participants (mean=0.285; SD = 0.035), as revealed by a two-sample t test (Fig. 2l, t = 82.04, $p < 0.001$). This association was consistently observed within all seven canonical networks for CU Aβ- (β-values ranging from 0.340 to 0.693, all $p < 0.001$; Supplementary Fig. 2a) and

Table 1 | Sample characteristics

Cross-sectional sample					
	CU Aβ- (n = 54)	**CU Aβ + (n = 9)**	**MCI Aβ + (n = 28)**	**Dementia Aβ + (n = 54)**	***P* value**
Age, years	65.15 (7.95)	70.67 (5.85)	71.21 (9.18)	68.57 (7.64)	0.007
Sex, (male/female)	15/39	2/7	12/16	21/33	0.391
Education, years	13.03 (2.67)	12.78 (3.03)	12.20 (3.48)	9.52 (3.47)	3.84×10^{-7}
MMSE	28.68 (1.36)	27.22 (2.28)	26.19 (1.71)	15.47 (5.30)	7.38×10^{-42}
ApoE ε4 status (pos/neg)	14/39	3/5	16/12	33/19	0.001
Longitudinal sample					
	CU Aβ + (n = 2)	**MCI Aβ + (n = 7)**	**Dementia Aβ + (n = 9)**		***P* value**
Age, years	73.00 (4.24)	71.14 (7.84)	72.11 (8.12)		0.946
Sex, (male/female)	1/1	1/6	3/6		
Education, years	14.00 (2.83)	10.71 (4.50)	10.00 (2.92)		0.393
MMSE	28.00 (2.83)	25.86 (1.77)	17.67 (5.31)		0.002
ApoE ε4 status (pos/neg)	1/0	5/2	6/3		
SV2A-PET follow-up years	1.07 (0.05)	1.22 (0.38)	1.17 (0.13)		0.766

The two -sided *p* values for continuous variables are determined by the ANOVA test, and those for categorical variables are determined by the chi-square test.
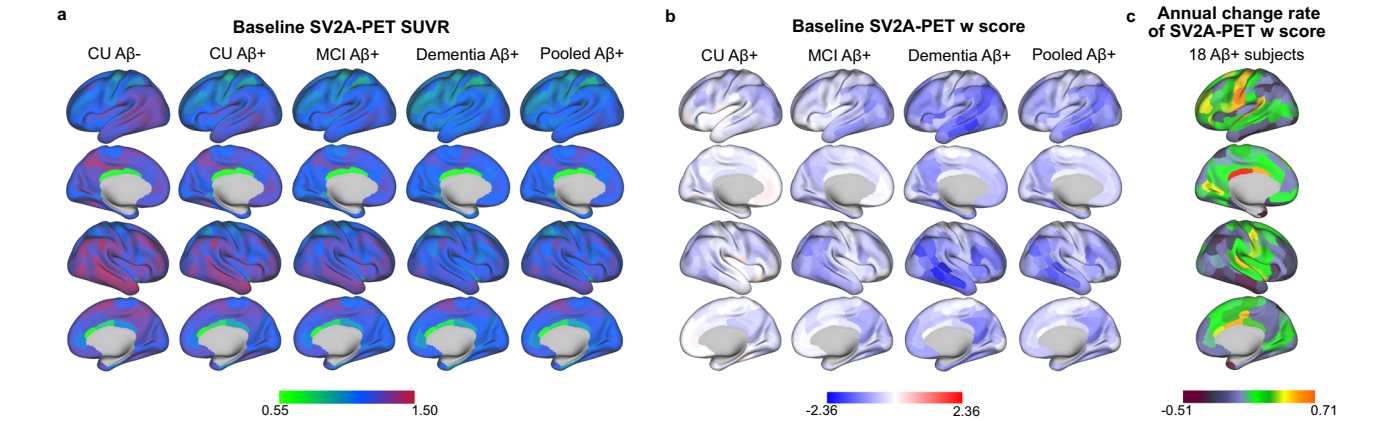*MMSE* Mini-Mental State Exam.

Fig. 1 | Group-average SV2A-PET SUVR, SV2A-PET w score and annual change rate of SV2A-PET w score. a Group-average SV2A-PET SUVRs. **b** Group-average SV2A-PET w scores. **c** Group-average annual change rates of SV2A-PET w score. The maps are rendered on cortical surfaces, stratified by diagnostic groups (i.e., CU Aβ-, CU Aβ + , MCI Aβ + , Dementia Aβ+ participants, and pooled Aβ+ participants).

Annual change rates of SV2A-PET w scores were measured in a subset of 18 Aβ+ participants. SV2A synaptic vesicle glycoprotein 2A, SUVR standardized uptake value ratio, CU cognitively unimpaired, MCI mild cognitive impairment, Aβ amyloid-beta.

Aβ+ participants (β-values ranging from 0.406 to 0.738, all *p* < 0.001; Supplementary Fig. 2b). By repeating the analyses using the structural connectivity matrix in Aβ+ subjects, we also observed the association between structural connectivity and SV2A-PET w-score covariance (Fig. 2k, β = 0.425, $p_{rewired}$ < 0.001). Paired t-tests on the bootstrapped β values showed significantly higher association with functional connectivity (FC) matrix compared to structural connectivity (SC) matrix (Fig. 2m, t = 10.07, *p* < 0.001), suggesting that functional connectivity contributes more to explain SV2A-PET w scores covariance compared with structural connectivity.

To avoid that the association between SV2A w-score covariance and the functional connectivity in Aβ+ subjects was driven by the network-like pattern of natural interindividual variation, we tested the association, additionally controlling for the SV2A-PET SUVR covariance across CU Aβ- subjects, and found a congruent result (β = 0.262, $p_{rewired}$ < 0.001). To further avoid the possibility that the association was driven by the physical proximity between ROIs, we additionally controlled the model with the inter-regional Euclidean distance; results remained consistent (Supplementary Fig. 3).

The pattern of synaptic density loss is constrained by network topology

Next, we tested whether synaptic loss pattern was shaped by network organization by adopting to the network spreading approach described previously[40,41]. Briefly, we hypothesized that regional synaptic loss is associated with the collective levels of synaptic loss in the neighbors weighted by interregional connectivity. We calculated for each ROI the connectivity-weighted SV2A-PET w score following the formula in network spreading model (Fig. 3a). The network was defined based on functional connectivity networks with sparsity levels ranging from 25% to 100% and the structural connectivity network. Then we assessed the association between the regional SV2A-PET w scores and connectivity-weighted SV2A-PET w score across the remaining connected ROIs, e.g., the functional connectivity-weighted mean neighbor w score is positively related to the regional SV2A w score under the network sparsity of 75% (Fig. 3c, β = 0.567, *p* < 0.001). In order to test the significance of observed association, we compared the model against two null models (Fig. 3b). The first null model was to verify the spatial association is not induced by spatial autocorrelation. The SV2A-PET w-score map was
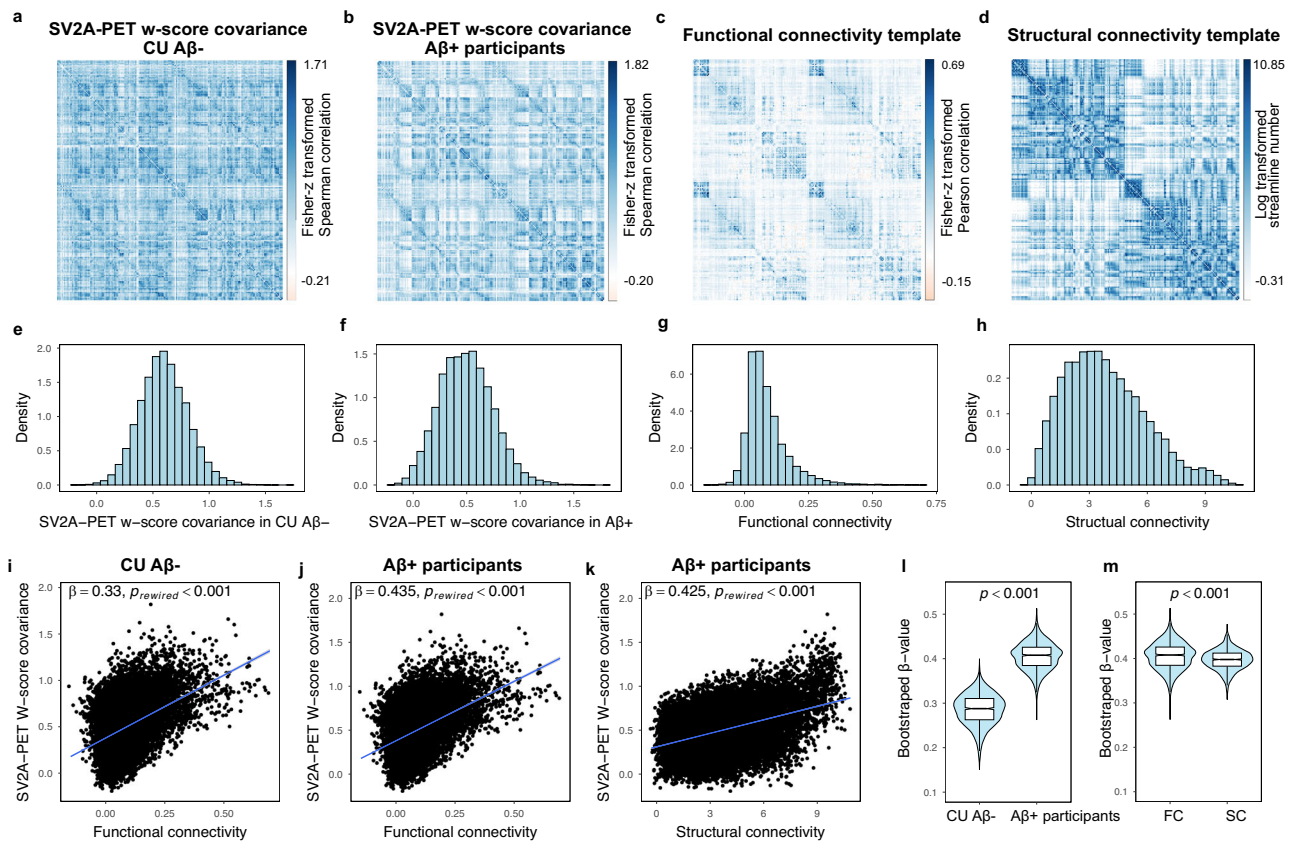
Fig. 2 | Associations between brain connectivity and covariance in SV2A-PET w scores. Covariance matrices of SV2A-PET w scores in CU Aβ- subjects (**a**, n = 54) and Aβ+ participants (**b**, n = 91). Group-average Fisher-z-transformed functional connectivity (FC) matrix (**c**) and log-transformed structural connectivity (SC) matrix (**d**) from 58 CU subjects with no evidence of abnormal amyloid-PET or tau-PET binding. (**e-h**) Density plots illustrated the distribution of the SV2A w-score covariance and brain connectivity. Scatterplots show the relationship between group-average functional connectivity and the covariance of the SV2A-PET w score in the CU Aβ- (**i**) and Aβ+ participants (**j**), as well as the relationship between structural connectivity and SV2A-PET w score covariance in Aβ + (**k**). β values were estimated by linear regressions. All two-sided p values estimated from linear regression models are $<2.2 \times 10^{-308}$. Linear model fits are indicated with 95% confidence intervals. To validate this association against the network topology, a one-sided permutation

was performed by comparing the exact regression-derived β value against the null distribution from 1000 rewired network matrices (all $p_{rewired} < 0.001$). **l** The associations between functional connectivity and SV2A w-score covariance in CU Aβ- and Aβ+ participants were compared by two-sample t-test from 1000 bootstrapped samples (two-sided $p < 2.2 \times 10^{-308}$). **m** The associations derived from functional connectivity and structural connectivity in Aβ+ subjects were compared by paired t-test from 1000 bootstrapped samples (two-sided $p = 4.25 \times 10^{-23}$). Boxes represent the interquartile range, with the median indicated by the center line. The bounds of the box correspond to the 25th and 75th percentiles. Whiskers extend to the minimum and maximum values within 1.5 interquartile range. FC functional connectivity, SC structural connectivity. Source data are provided in a Source data file.

projected to the spherical surface and randomly rotated for 1000 times to generate 1000 surrogate maps (i.e. null spin). The second null model was to verify the spatial association was not induced by network topology. The connectivity matrix was shuffled for 1000 times with preserved network degree and weight to generate 1000 surrogate networks (i.e. null rewired). The p-value was determined by comparing the observed β value with the null distribution of β values. The observed association using functional network under different network sparsity as well as structural network was consistently better than that from two null models (Fig. 3d, FC 100% sparsity: $β = 0.364$; FC 75% sparsity: $β = 0.411$; FC 50% sparsity: $β = 0.475$; FC 25% sparsity: $β = 0.567$; SC: $β = 0.300$; all p_{spin} and $p_{rewired} < 0.001$). At the subject level, the subject-derived β values were significantly greater than zero at each network sparsity (Fig. 3e, FC 100% sparsity: mean $β = 0.311$; FC 75% sparsity: mean $β = 0.343$; FC 50% sparsity: mean $β = 0.387$; FC 25% sparsity: mean $β = 0.450$; SC: mean $β = 0.350$; all $p < 0.001$). Congruent results were obtained when controlling for the natural distribution pattern of synaptic density (i.e., the group-average SV2A-PET SUVR from CU Aβ− subjects) as well as mean Euclidean distance to each ROI (Supplementary Fig. 4). More information can be found in Supplementary Table 2. These results collectively confirm that the pattern of

synaptic loss is constrained by the network, with a stronger association with the functional network. To verify whether this relationship is exacerbated in AD, we repeated the individual-level analysis in the CU Aβ− subjects and compared with the Aβ+ subjects. The results showed that at each FC sparsity level and in the SC network, the associations were consistently higher in the Aβ+ group than in the CU Aβ− group, after controlling for age, sex, education level, and clinical diagnosis (Fig. 3f).

To further explore whether the observed association is impacted by APOE4 status, we compared the subject-level associations between APOE4 carriers and noncarriers. No significant difference was found across functional network sparsity and structural network (Supplementary Fig. 5).

Functional connectivity to the epicenter is associated with group-average synaptic loss

We then tested whether the pattern of synaptic loss can be modeled by the connectivity to the synaptic loss epicenter (i.e. the putative initial site of synaptic loss). Since functional connectivity outperformed structural connectivity in aforementioned results, we focused on functional connectivity in the following analyses. The epicenter was
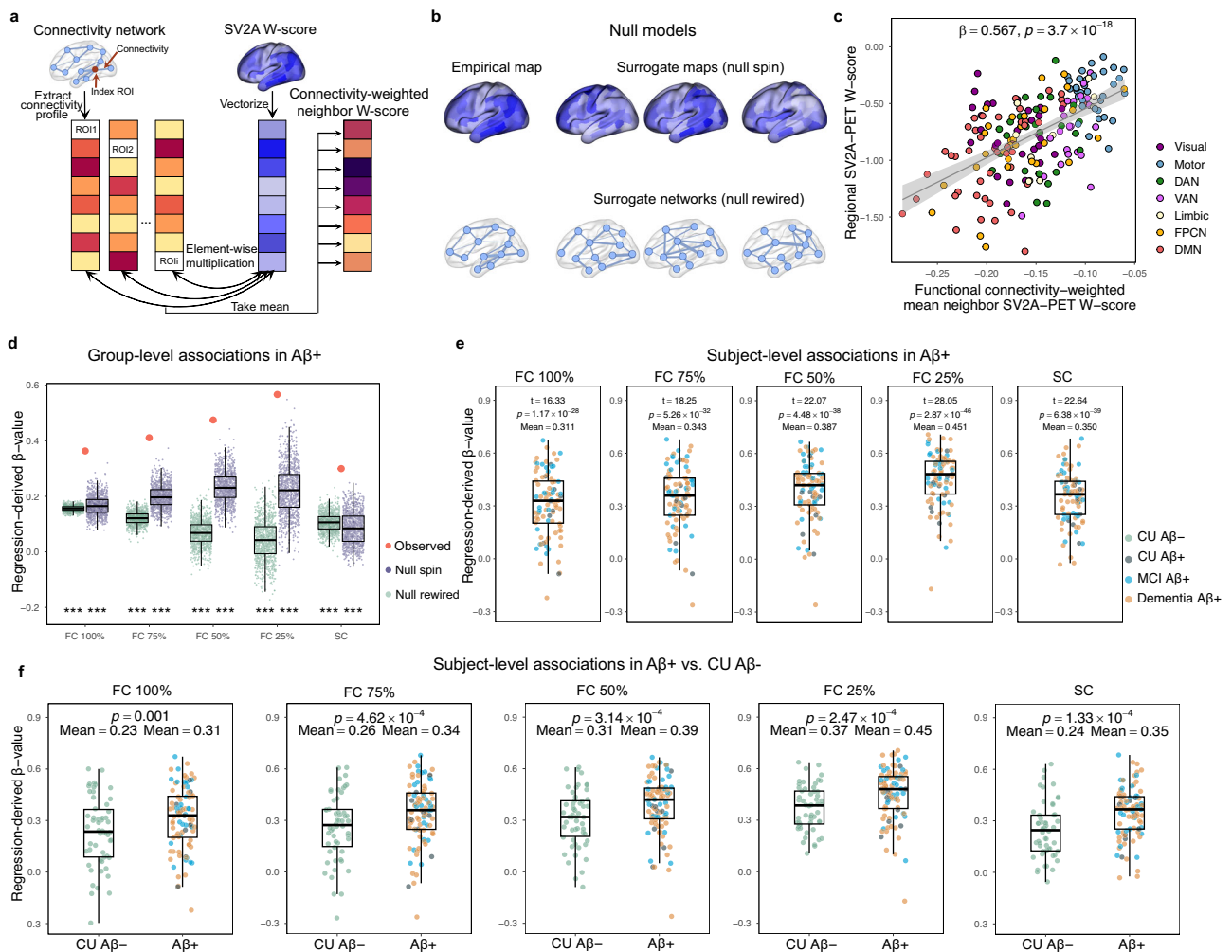
Fig. 3 | Associations of regional synaptic loss with the brain network connectome. a Schematic illustration of the model of network-associated synaptic loss. For a given index ROI (e.g., dark red), the SV2A-PET w score was modeled as the average of the w scores in the neighboring regions weighted by interregional connectivity. **b** The spatial association between the SV2A-PET w-score and averaged connectivity-weighted neighbor w-score was assessed against two null models accounting for autocorrelation (i.e., null spin) and network topology (i.e., null rewired). **c** As an example, the scatterplot shows the relationship between the group-average SV2A-PET w score in Aβ+ subjects (n = 91) and the functional connectivity-weighted neighbor w-score at the network sparsity of 25%, i.e., top 25% of connections with the strongest functional connectivity strength were preserved in the network. β and two-sided p value was derived from linear regression. The linear model fit is indicated with 95% confidence intervals. **d** The association was consistently significant compared to two null models (i.e., null spin and null

rewired) when using functional connectivity matrix across different network sparsity (i.e., from 100% to 25%) and structural connectivity in Aβ+ subjects. *** indicates one-sided $p_{rewired}$ or $p_{spin} < 0.001$, without adjustment for multiple comparisons. **e** The model was assessed for each participant. The significance of the subject-level β-value distribution among Aβ+ individuals was assessed using two-sided one-sample t-tests, without adjustment for multiple comparisons. **f** The comparisons of subject-specific associations between CU Aβ- (n = 54) and Aβ+ subjects were conducted using linear regressions adjusting for age, sex, and education years (all two-sided $p \leq 0.001$, uncorrected for multiple comparisons). Boxplots are displayed as median (center line) ± interquartile range (bounds) with whiskers including observations within the 1.5 interquartile range. ROI, region of interest. DMN, default mode network; FPCN, fronto-parietal control network; VAN, ventral attention network; DAN, dorsal attention network. Source data are provided in a Source data file.

primarily defined based on the assumption that regions showing substantial synaptic loss is potentially as an epicenter if it is also functionally connected to other regions experiencing great synaptic loss[40]. For each ROI, we calculated the mean rank of: (i) the regional SV2A-PET w-score; (ii) the mean of SV2A-PET w-score in the connected regions weighted by interregional connectivity. The epicenters were defined as those regions with significantly higher mean rank than the distribution of null ranks derived from 1000 spin models ($p_{spin} < 0.05$, Fig. 4a). At the group level, epicenters in Aβ+ participants were predominantly located in the parietotemporal cortex. The linear regression model revealed that greater functional connectivity to the SV2A-PET epicenter (Fig. 4b) was associated with lower SV2A-PET w-scores (i.e. greater synaptic loss) in connected brain regions ($\beta = -0.534$, $p_{rewired} < 0.001$, Fig. 4b) in pooled Aβ+ participants. Alternative

identification of epicenters (i.e., 5%, 10%, 20%, or 30% of ROIs with the lowest SV2A-PET w scores) following other previous studies[42,43] did not change the association at the group level (Supplementary Fig. 6). Controlling natural synaptic density distribution and Euclidean distance showed consistent results (Supplementary Fig. 7). Details can be found in Supplementary Table 3.

We further investigated whether the epicenter-based model remains effective across distinct distribution patterns, rather than being limited to the typical AD pattern. We performed hierarchical clustering on the SV2A-PET w-scores in Aβ+ subjects to stratify them into spatially distinct subtypes. Three spatial subtypes were found (Supplementary Fig. 8a), where predominant synaptic loss in the lateral and medial temporal lobe in subtype 1, in the peri-central cortex in subtype 2, and in the temporoparietal, occipitotemporal, and
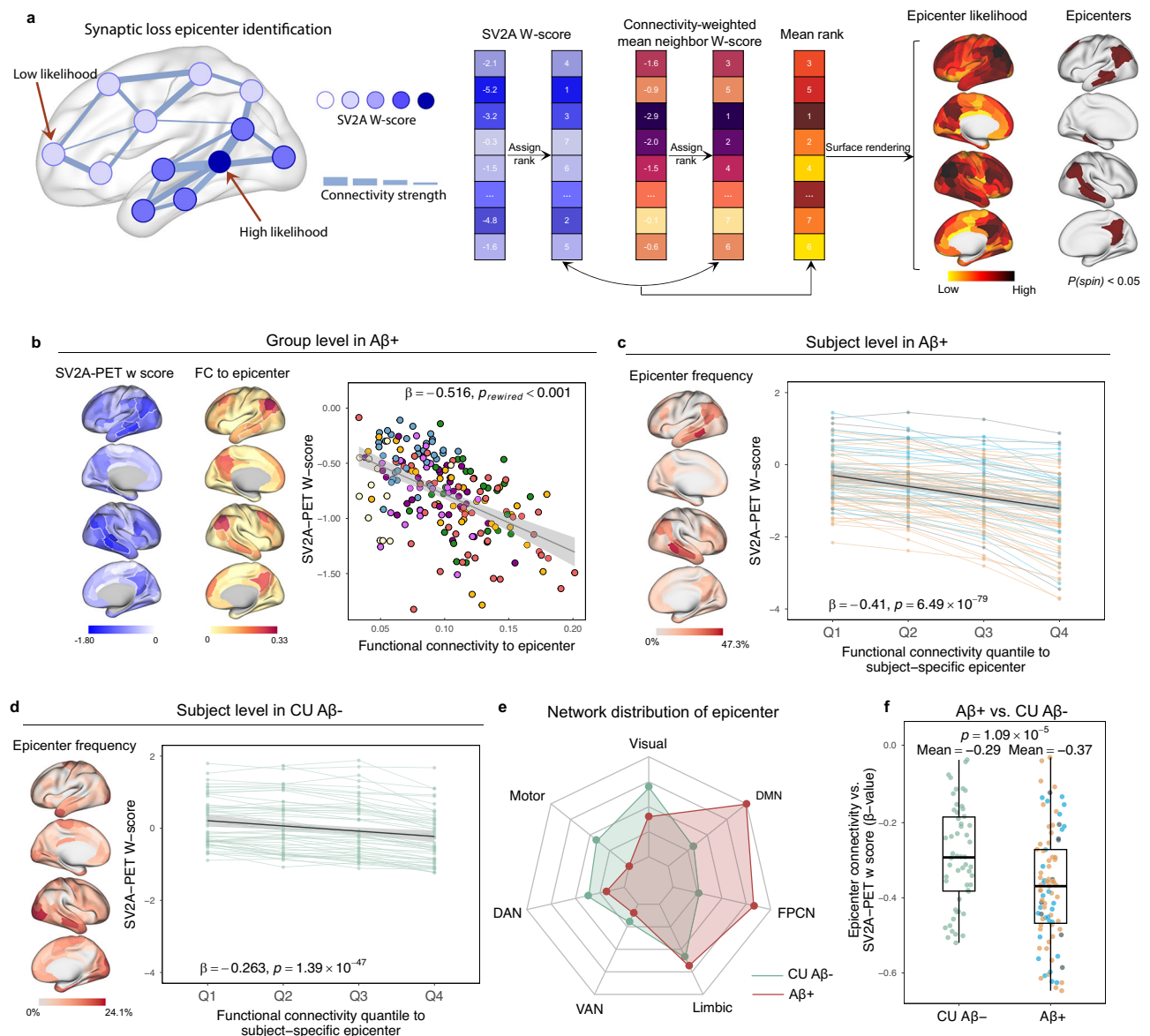
Fig. 4 | Epicenter connectivity-based prediction of cross-sectional synaptic loss. a A data-driven approach to identify the SV2A w score epicenter, adapted from the method proposed by Shafiei et al.[40]. Epicenter likelihood was calculated as the mean rank of the regional SV2A-PET w score and connectivity-weighted neighbor w score. ROIs with significantly higher mean ranks compared to the distribution of null ranks from 1000 surrogate maps were identified as epicenters (one-sided p_{spin} < 0.05, without multiple comparison correction). **b** Surface renderings show the group-average SV2A-PET w scores and epicenters functional connectivity (outlined in white) in Aβ+ group (n = 91). The association between SV2A-PET w score with epicenter connectivity was estimated by linear regression (p = 4.02×10⁻¹⁶, two-sided). To validate this association against the network topology, one-sided $p_{rewired}$ value was identified by comparing exact β value with the null distributions from the 1000 rewired connectivity matrices. **c** Subject-level epicenter connectivity-based prediction of SV2A-PET w score in Aβ+ subjects. Surface rendering illustrates the overlap frequencies of subject-specific epicenter locations. Based on functional connectivity quantities to the subject-specific epicenter, the

ROIs were divided into quartiles for each subject. Line charts show a gradual greater of synaptic loss across the ROIs weakly connected to the epicenters (i.e., Q1) to those strongly connected (i.e., Q4). β values and two-sided p values were estimated from linear mixed-effect regression models. **d** Subject-level epicenter connectivity-based prediction of SV2A-PET w score in CU Aβ- subjects (n = 54). **e** The epicenter probabilities were stratified according to the canonical functional networks in CU Aβ- (green line) and Aβ + (red line) groups. **f** A linear regression was applied for each subject to assess the association between subject-specific epicenter connectivity and SV2A-PET w-score. The subject-level regression-derived β values were compared between CU Aβ- and Aβ+ subjects using linear regression. Linear model fits are indicated with 95% confidence intervals. Boxplots are displayed as median (center line) ± interquartile range (bounds) with whiskers including observations within the 1.5 interquartile range. DMN default mode network, FPCN fronto-parietal control network, VAN ventral attention network, DAN dorsal attention network. Source data are provided in a Source data file.

precuneus in subtype 3. The functional connectivity to subtype-specific epicenters was consistently associated with group-average SV2A-PET w scores (Supplementary Fig. 8a, subtype 1: β = −0.432; subtype 2: β = −0.541; subtype 3: β = −0.622; all $p_{rewired}$ < 0.001). Sliding window analyses simulated distinct spatiotemporal trajectories of

synaptic loss across subtypes with consistent associations between epicenter connectivity and SV2A-PET w-scores observed at each time window (Supplementary Fig. 8b; Supplementary Table 4). These results collectively indicate that synaptic loss pattern follows the connectivity patterns to spatially heterogeneous epicenter locations.
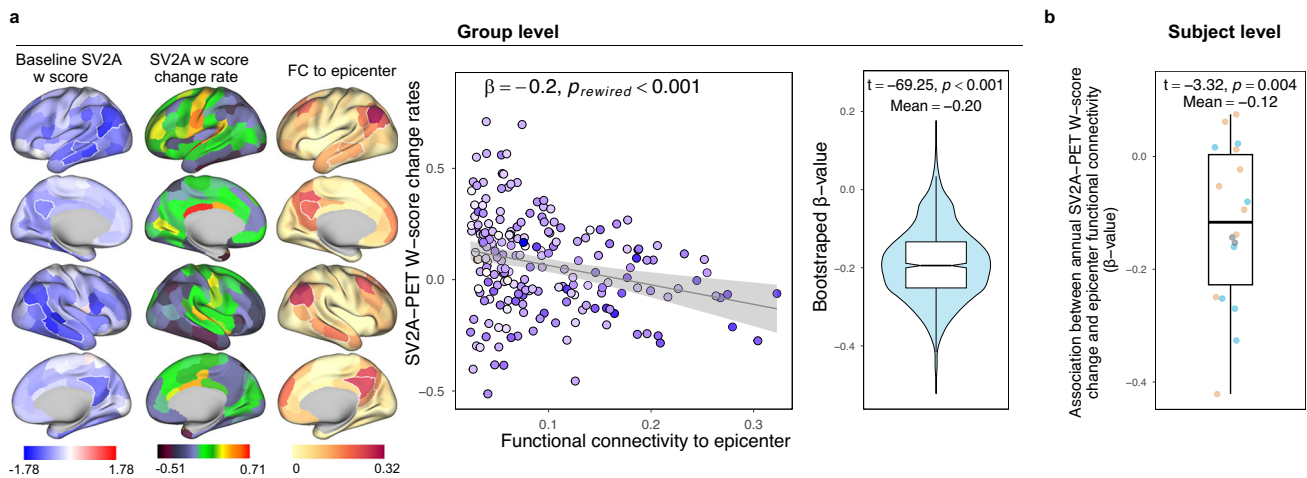
Fig. 5 | Association between functional connectivity to baseline epicenter and longitudinal changes in SV2A-PET w score in a subset of 18 Aβ+ participants. a The group-level linear regression model was applied to assess the association between functional connectivity to group-level baseline epicenter and group-average annual change rates of SV2A-PET w-score in Aβ+ participants (n = 18), controlling for the baseline SV2A-PET w score ($\beta = 0.20$, two-sided $p = 0.009$). To validate this association against the network topology, a one-sided permutation was performed by comparing the exact regression-derived β value against the null distribution from 1000 rewired network matrices ($p_{rewired} < 0.001$). Linear model fits are indicated together with 95% confidence intervals. The group-level association is assessed iteratively on 1000 bootstrapped samples. The distribution of resulting β-values is tested using a one-sample t-test (two-sided $p < 2.2 \times 10^{-308}$). **b** Subject-level analysis of individual synaptic density change rates was applied for each subject with subject-specific epicenters. The significance of the distribution of linear regression-derived β-values was tested using a one-sample t test (two-sided $p = 0.004$). Boxplots are displayed as median (center line) ± interquartile range (bounds) with whiskers including observations within the 1.5 interquartile range. Source data are provided in a Source data file.

Functional connectivity to subject-specific epicenters is associated with individual variability in synaptic loss

To further determine whether the epicenter-based model also accounts for inter-individual heterogeneity in synaptic loss, we extended our analyses to the subject level. We determined the subject-specific synaptic loss epicenter for each Aβ+ participants. Considerable interindividual variability in the locations of epicenters was observed among pooled Aβ+ participants (see surface renderings in Fig. 4c), with a maximum 47.3% overlap frequency of subject-specific epicenters. The cortical ROIs were stratified into 4 quantiles according to their mean connectivity to the epicenter ROIs (i.e., Q1-Q4 ROIs), where Q1 ROIs had the weakest functional connectivity strength to the epicenter, while the Q4 ROIs had the strongest functional connectivity to the epicenter. The mean SV2A-PET w scores across the ROIs of each quantile were subsequently computed for each participant. The linear mixed effect regression model demonstrated that the strength of functional connectivity to the epicenter was associated with individual SV2A-PET w scores in the connected Q1-Q4 ROIs (Fig. 4c, $\beta = -0.410$, $p < 0.001$), accounting for the fixed effects of age, sex, clinical diagnosis, and education years and random intercepts. Additionally, including APOE4 status as a covariate did not alter the subject-level association between epicenter connectivity and SV2A-PET w score ($\beta = -0.409$, $p < 0.001$). Replication with alternative identification (i.e., 5%, 10%, 20%, or 30% of ROIs with the lowest SV2A-PET w scores) showed consistent results (first column in Supplementary Fig. 9). Subject-level analyses reinforced the view that synaptic loss distribution in AD aligns with the connectivity pattern to epicenters.

To test the robustness of subject-level modeling, we computed the subject-level association of SV2A-PET w-score and connectivity to subject-specific epicenter (i.e., subject-level regression-derived β value) for each Aβ+ subject, and compared the actual β value with the distribution of 1000 β values from two null modes (i.e., null spin and null rewired). As shown in Supplementary Fig. 10, the actual model of 88 subjects out of 91 Aβ+ subjects (97%) outperformed the null rewired models, and 82 (90%) subjects outperformed the null spin models. These results indicate that the majority of subjects showed prediction performance beyond what would be expected by chance.

To further confirm that the pattern of synaptic loss in AD patients more closely follows the epicenter connectivity model compared to CU Aβ- individuals, we also analyzed the relationship between SV2A-PET w-scores and the functional connectivity of subject-specific epicenters in the CU Aβ- group. While synaptic density alterations (i.e., SV2A w scores) in CU Aβ- individuals were also associated with the epicenter connectivity (Fig. 4d), this association was weaker than that observed in the Aβ+ group. Furthermore, the CU Aβ-group exhibited a lower epicenter overlap probability, with a maximum overlap frequency of 24.1%, and a relatively uniform distribution across functional networks. Notably, epicenters were more prevalent in the visual and limbic networks, a pattern distinct from that observed in the Aβ+ group, where the epicenters were more commonly found in default mode network (DMN), frontoparietal control network (FPCN) and limbic network (Fig. 4e). We then computed the subject-specific association between epicenter connectivity and individual SV2A-PET w-scores using subject-level linear regression, and compared the distribution of these subject-level associations (i.e., β values) between CU Aβ- and Aβ+ groups. The results revealed that the epicenter-based associations of synaptic loss in Aβ+ subjects were stronger than in CU Aβ- subjects (Fig. 4f). These findings suggest that in CU Aβ- individuals, the pattern of synaptic density alterations driven by non-AD factors, may differ from that in the AD patients. AD appears to introduce a spatial pattern of synaptic loss that more closely aligns with functional connectivity to individual epicenters.

Subject-level analyses for spatial subtypes (Supplementary Fig. 8c-e) and with alternative identification of epicenter (column 2-4 in Supplementary Fig.9) yielded consistent results. Furthermore, no significant difference of the subject-level epicenter connectivity-based synaptic loss between APOE4 carriers and noncarriers in Aβ+ subjects (Supplementary Fig. 11).

Stronger connectivity to baseline synaptic loss epicenter is associated with accelerated longitudinal synaptic loss

For a subset of 18 Aβ+ participants who underwent longitudinal SV2A-PET scan, we assessed whether functional connectivity to synaptic loss epicenters identified by baseline SV2A-PET w-score map is associated with future change rates in SV2A-PET w-scores. As expected, stronger
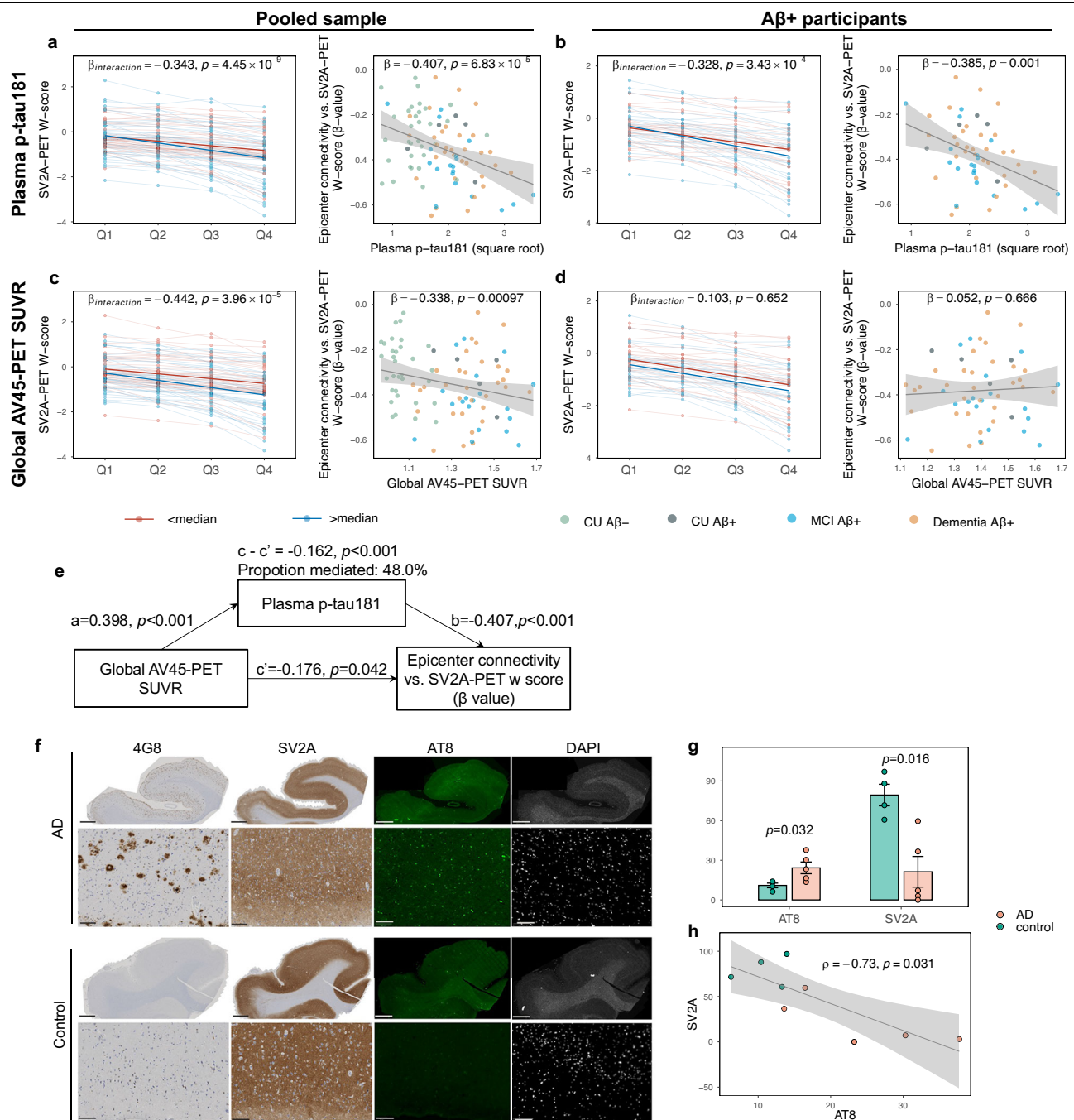
Fig. 6 | The effect of p-tau and Aβ on connectivity-mediated synaptic loss. The line charts illustrated the interaction effect estimated from linear mixed effect regressions between plasma p-tau181 level and the functional connectivity (i.e., Q1-Q4) to epicenters (first row) on mean SV2A-PET w-scores, and global AV45-PET SUVR and functional connectivity to epicenters on mean SV2A-PET w-scores (second row) respectively in pooled sample (**a, c**, n = 88) and Aβ+ subjects (**b, d**, n = 56). The scatterplots show that associations estimated from linear regressions between connectivity-based SV2A-PET w-score (β values derived from subject-level linear regression) and the concentration levels of plasma p-tau181 (first row), as well as global AV45-PET SUVR (second row), respectively among pooled sample (**a, c**) and Aβ+ subjects (**b, d**). **e** The mediation effect of plasma p-tau181 concentration on the association between global AV45-PET SUVR and connectivity-based SV2A w-score

among the pooled sample. **f** The presence of Aβ plaques (4G8 staining), relatively lower intensities of SV2A, and tau (AT8 staining, green) in postmortem brain tissue of entorhinal cortex from AD patients (n = 5) than in the controls (n = 4). Nuclei were counterstained with DAPI (white). Scale bars = 2000 μm (row 1, 3) and 50 μm (row 2, 4). **g** Significantly reduced levels of SV2A and increased levels of AT8 were found in the entorhinal cortex of AD patients compared to those in the controls indicated by Mann-Whitney test. Bar heights represent group means, and error bars represent ±1 standard error of the mean (SEM). **h** The association between the levels of AT8 and SV2A is tested using Spearman correlation. Linear model fits are indicated together with 95% confidence intervals. The statistical significance is assessed using two-sided tests. Source data are provided in a Source data file.

functional connectivity to baseline epicenter is associated with greater annual change rates of synaptic loss in connected brain regions at group level (Fig. 5a, $\beta = -0.200$, $p_{rewired} < 0.001$), controlling for baseline SV2A-PET w scores. To test the significance, we iteratively repeated

this analysis on 1000 bootstrapped samples (i.e., random sampling with replacement from pool sample). The distribution of β-values from 1000 bootstrapped samples was significantly lower than zero ($t = -69.25$, $p < 0.001$, mean $= -0.20$). At subject-level, consistent result

was evidenced by a significantly negative β-value distribution derived from subject-level linear regression models of the annual change rate of SV2A-PET w-scores against subject-specific baseline epicenters (Fig. 5b, t = −3.68, p = 0.002, mean = −0.12). Additionally, controlling for the Euclidean distance yielded consistent results (t = −3.32, p = 0.004, mean = −0.11). Bootstrapped associations using functional connectivity are stronger than structural connectivity at the group level (FC: mean = −0.20; SC: mean = −0.18; p = 0.002), while this association was not significantly different at the subject level (FC: mean = −0.12; SC: mean = −0.08; p = 0.422).

The connectivity-mediated synaptic loss is influenced by phosphorylated tau and amyloid-β

Last, we tested whether and how connectivity-based synaptic loss is influenced by amyloid and pathological tau. To this end, we included a subset of 88 subjects who were additionally tested for plasma p-tau181 concentrations, comprising 32 CU Aβ- and 56 Aβ+ subjects (For demographics see Supplementary Table 5). Linear mixed effect model revealed that both plasma p-tau181 concentration showed significant interaction effect with functional connectivity of quartile ROIs to epicenter on the level of SV2A-PET w-score in pooled sample as well as Aβ+ group (Fig. 6a, b), suggesting the synaptic loss is more profound along the functional connectivity to epicenter in the subject with higher plasma p-tau181 concentration. Global AV45-PET SUVR showed a significant interaction effect with functional connectivity on the level of SV2A-PET w-score in pooled sample but not in Aβ+ group (Fig. 6c, d). Then, we assessed the association between plasma p-tau181 levels and global AV45-PET SUVR and subject-level connectivity-mediated SV2A-PET w score (i.e., subject-level linear regression-derived β values). Higher plasma p-tau181 concentration was significantly associated with stronger connectivity-mediated SV2A-PET w score in the pooled sample (Fig. 6a, $\beta = -0.407$, $p < 0.001$) as well as Aβ+ subjects (Fig. 6b, $\beta = -0.385$, $p < 0.001$). Global AV45-PET SUVR was only significantly associated with connectivity-mediated SV2A-PET w score in the pooled sample (Fig. 6c, $\beta = -0.338$, $p < 0.001$), but not in Aβ+ subjects (Fig. 6d, $\beta = 0.052$, $p = 0.666$). Mediation analyses revealed that plasma p-tau181 concentration partially mediated the effect of global AV45-PET SUVR on connectivity-mediated SV2A-PET w score (Fig. 6e). Congruent results were observed when additionally including APOE4 status as a covariate (Supplementary Fig. 12).

We further verified whether the tau pathology is linked to lower synaptic density in the post-mortem tissue from 5 AD patients and 4 normal control subjects, confirmed by clinical diagnosis and pathological examination. The post-mortem entorhinal cortex brain blocks were collected from the Netherlands Brain Bank (Fig. 6f, Supplementary Table 6). We chose the entorhinal cortex for analyses since it has been suggested as the stereotypical initial region of tau pathology by Braak staging[44]. Significant increases in AT8-immunoreactive p-tau and a decrease in SV2A levels were detected in the AD patients compared to the controls (Fig. 6g). Higher levels of AT8 were related to SV2A levels in the entorhinal cortex (Fig. 6h). Together, these results supported that p-tau may relate to synaptic loss and promote the connectivity-mediated synaptic loss.

Discussion

In this combined cross-sectional and longitudinal study, we demonstrated the synaptic loss distribution is partially constrained by brain network topology, and is modulated by p-tau in AD. We combined SV2A-PET-assessed synaptic loss in a group of 91 subjects with abnormal amyloid-PET binding and a template-based functional connectome from a group of 58 CU subjects with no evidence of PET-assessed abnormality in amyloid and tau. First, we found that strongly connected regions exhibited shared levels of synaptic loss. Second, the regions with greater synaptic loss were more strongly connected to other regions with greater synaptic loss. Third, the cross-sectional

synaptic loss pattern and longitudinal synaptic loss rates could be modeled by a normative functional connectivity pattern to synaptic loss epicenters at both the group level and the subject level. The epicenter connectivity-based modeling can be generalized to spatially heterogeneous synaptic subtypes. AD appears to exacerbate the network-constrained synaptic alterations and exhibit distinct origins compared to CU Aβ- subjects. These results provided evidence that synaptic loss initiates in heterogeneous local brain regions (i.e., synaptic loss epicenters) in AD patients, but the brain-wide synaptic loss can be modeled as a function of functional connectivity to the initial regions experiencing synaptic loss. Last, by analyzing the plasma concentration of a subset of participants, we found higher levels of p-tau181 and global AV45-PET SUVR are associated with greater synaptic loss along the epicenter connected regions in pooled sample covering both Aβ- CU and Aβ+ individuals, while p-tau181 appears to play a more direct role in connectivity-mediated synaptic loss, especially in individuals already showing amyloid burden. Postmortem data also supported the correlation between AT8 (i.e. p-tau) and SV2A in entorhinal cortex tissue which is believed to be one of the initial regions affected in AD. Together, our findings contribute to the growing understanding that synaptic loss in AD may be partially shaped by brain connectome topology, with pathological tau playing a key role in connectivity-constrained mechanism. However, an exact causal relationship requires future longitudinal and mechanistic studies.

Our major finding is that the topology of the functional network may influence the distribution of synaptic loss. We showed that the levels of synaptic loss covaried across functionally close regions and were associated with collective levels of synaptic loss in connected regions, suggesting that synaptic loss preferentially propagates across connected regions. The synaptic loss covariance captures interregional similarity and network-level associations, which could potentially reflect the synchronization of synaptic loss. Evidence has indicated that functional networks assessed by fMRI signals are underpinned by particular gene expression profile primarily encoding ion channels, and correlated with PET-assessed synaptic density, indicating that the functional network is tightly related to the machinery of synaptic communication[10,45]. Synaptic density networks derived by common covariance across subjects in the human brain partly align with resting-state fMRI networks[14,46] Similarly, highly interconnected regions were found to show shared metabolic alterations[47], similar gene expression profiles[48], and molecular properties[49,50]. Therefore, the synaptic loss pattern may be, to a certain degree, shaped by the brain network architecture due to similar molecular biological characteristics between connected regions, leading to shared susceptibility to AD pathology[51,52]. It is critical for future studies to explicitly address the association between tau accumulation or molecular modulating factors (i.e., gene expression, neurotransmitter receptors, etc.) and connectivity-mediated synaptic loss in AD.

It is pivotal to note that the network-based pattern of synaptic density alteration observed in Aβ+ individuals may not be entirely specific to AD. Though significantly weaker, associations between SV2A w-scores and network topology were also observed in CU Aβ-controls. However, these deviations in the control subjects were generally subtle, non-directional, and likely reflect non-pathological individual variability. This may arise from unknown factors such as genetic differences, environmental exposures, or normal developmental processes[53–56]. In contrast, Aβ+ individuals exhibited spatially structured, predominantly negative deviations, reflecting widespread synaptic loss that aligns with the brain network topology. Although the strength of the association with network topology in AD was only moderately higher than in controls, this modest increase may reflect a different mechanism. It suggests that AD pathology induces synaptic degeneration more closely aligning with network

architecture, rather than an amplification of normal variability. These findings support the view that network topology contributes to the spatial pattern of synaptic density alteration and highlight an important direction for future investigation, that is the extent to which brain connectivity shapes the distribution of synaptic density alterations across normal aging and distinct pathological conditions.

While we observed a significant association between SV2A w-scores and brain network topology in the AD group, this relationship should not be directly interpreted as evidence of active network-based propagation of synaptic loss. Rather, the observed spatial alignment between synaptic loss and connectivity may partly reflect the impact of tau pathology propagating along intrinsic brain networks. Recent translational studies have indicated correlated tau accumulation in compactly connected brain regions by linking the tau-PET abnormalities to functional network architecture in AD[33,57]. In particular, tau-PET signal increases have been shown to follow the connectivity to early epicenters such as the entorhinal cortex or inferior temporal lobe[34,58]. Importantly, converging evidence indicates that pathological tau can directly damage synapses via toxicity to intracellular synaptic proteins, many of which are presynaptic vesicle proteins, such as SV2A, leading to synapse loss both locally and at distal sites[59–61]. Several multimodal studies combining tau-PET and SV2A-PET have demonstrated inverse associations between tau-PET uptake and SV2A-PET signals, including tau burden in the entorhinal cortex with synaptic loss in hippocampus in AD patients[25], as well as in medial temporal in amnestic MCI[23], in line with post-mortem observations showing that synaptic protein expression is lower in neurons with NFTs than in those without NFTs[62]. Baseline tau-PET levels are found to be negatively associated with longitudinal SV2A loss in early Braak regions[63]. These findings collectively support a crucial role of tau spreading in shaping the network-constrained distribution of synaptic loss in AD. However, tau pathology alone may not fully explain the observed spatial pattern. Several studies in AD[24] and primary tauopathies (progressive supranuclear palsy and corticobasal degeneration)[64] have reported a bidirectional, non-linear, and stage-dependent relationship between tau burden and SV2A binding, suggesting that their association varies across disease progression rather than is uniformly negative. Furthermore, recent PET studies have demonstrated that SV2A-PET exhibits a distinct alteration pattern compared to tau[23,24,65], although they are partially overlapped. For example, substantial synaptic loss in regions typically spared by fibrillar tau has been identified, including the peri-central cortex and occipital lobe[22,25,66], consistent with the subtype2 pattern observed in the current study. These findings collectively suggest that while tau spreading may play a major role, it may not fully account for the spatial distribution of synaptic loss in AD. Future work should aim to clarify the extent to which tau pathology contributes to the observed network-constrained patterns of synaptic loss, and to distinguish tau-driven mechanisms from intrinsic network vulnerability.

Among the tau species, soluble tau has been indicated to induce primary toxicity to synapse, which is evidenced by the fact that purified soluble tau induced greater synaptic loss to mouse neuron culture[67]. Our findings demonstrate a link between plasma p-tau181 and connectivity-mediated synaptic loss in both the pooled sample and Aβ+ individuals. Although Aβ is highly toxic to synapses, its association with connectivity-mediated synaptic loss was only evident in the pooled sample. Similarly, a recent study also reported a greater effect of CSF p-tau on CSF presynaptic growth-associated protein 43 (GAP-43) than Aβ-PET[68]. Moreover, we observed that the relationship between Aβ-PET and connectivity-based synaptic loss was partially mediated by plasma p-tau181, supporting previous evidence that Aβ-induced synaptic damage occurs in a tau phosphorylation-dependent manner[21,69,70]. Building on prior findings that tau and Aβ contribute to overall synaptic loss (particularly as measured by CSF GAP-43)[68,71], we

extend this understanding using SV2A-PET to show how tau and Aβ influence the relationship between synaptic loss and connectivity patterns. Our results highlight the central role of pathological tau in the connectivity-based propagation of synaptic loss. These findings further support the recent hypothesis[17], suggesting that, in the early stages of amyloid accumulation, synaptic loss is confined to the vicinity of the plaques, which is later exacerbated by pathological tau, and propagates to widespread regions when both pathologies advance. A recent pre-clinical study reported a potential off-target interaction between UCB-J SV2A ligand and p-tau, particularly in the nucleus[72], which leads to the possibility that the UCB-J could either directly bind to p-tau or indirectly via SV2A binding to p-tau. Indeed, pathological tau has been shown to bind to synaptic vesicles and interfere with presynaptic functions[59]. Therefore, this potential direct binding to tau could confound the interpretation of the network-based pattern of synaptic loss and tau spread. Tau pathology binding to synaptic vesicles may indirectly cause patterns resembling tau propagation due to synaptic vesicle damage. However, pre-blocking with a tau ligand only resulted in a 22% reduction in UCB-J signal, and off-target interactions were observed exclusively in the nucleus.

Importantly, the connectivity-based prediction is capable of capturing the heterogeneity of synaptic loss in AD. We found that the Aβ+ subjects could be grouped into three spatially distinct subtypes with distinct severity-dependent propagation trajectories, where the distinct synaptic loss pattern of each subtype is consistently associated with connectivity to the subtype-specific epicenters. Another strength of the current study was that we extended our findings toward subject-level data. The levels of regional synaptic loss gradually increased with functional connectivity to subject-specific epicenters, which replicated and reinforced the results at the group level. Our subject-level modeling suggests the potential for developing individualized predictive models in future studies. Future research could incorporate subject-specific data, such as baseline fMRI, SV2A-PET, and clinical factors, to map personalized connectivity patterns and synaptic loss, enabling more accurate predictions of disease progression. Such individualized models could help identify regions with a higher likelihood of greater synaptic loss, which may enhance the sensitivity of detecting treatment effectiveness compared to stereotypically vulnerable regions (e.g., the medial temporal lobe and whole brain). Additionally, these models could aid in stratifying patients based on their predicted synaptic loss patterns, ensuring that treatments are tested on subgroups most likely to benefit. Furthermore, deviations between predicted and observed synaptic loss could serve as a quantitative biomarker for assessing treatment impact, offering a more sensitive measure of intervention effectiveness and facilitating more adaptive trial designs.

Several caveats should be considered when interpreting the findings of this study. First, the w-score used to quantify synaptic alterations does not directly reflect absolute or biologically synaptic loss. In the AD group, it captures region-wise deviations from the normative mean derived from CU Aβ- controls and thus represents relative synaptic density difference. In contrast, w-scores observed in CU Aβ- individuals likely reflect intra-individual variability, the mechanisms of which remain uncharacterized. These deviations may arise from heterogeneous, non-pathological influences and should not be interpreted as reflecting synaptic pathology. Second, while the observed associations consistently showed statistical significance, it is important to emphasize that statistical significance does not equate to biological relevance or mechanistic strength. The effect sizes of the observed in this study were generally modest, and should be interpreted as indicating the presence of spatially organized patterns of synaptic loss, rather than definitive evidence of underlying causal mechanisms. Future studies with larger samples, longitudinal follow-up, and multimodal pathological markers will be necessary to further elucidate the biological drivers of these connectivity-based effects.

The strength of this study was that we integrated cross-sectional and longitudinal data, incorporating both group-level and subject-level analyses, and combined neuroimaging, plasma, and postmortem data. Furthermore, combining subtype-, and subject-specific connectivity-based predictions can sensitively capture spatial heterogeneity in synaptic loss in AD patients. There are several limitations in this study. First, due to the limited sample size of the longitudinal data included in this study, the association between functional connectivity and synaptic loss change rates should be further validated with a larger sample size. In addition, future studies could focus on developing individualized predictive models that forecast future synaptic loss based on baseline functional connectivity. Second, these data were only obtained from one center, and external validation would strengthen our findings. However, limited centers are collecting SV2A-PET data, especially with larger samples with the same SV2A PET tracer. Third, we used a normative connectivity template rather than subject-specific connectivity. While this approach ensures consistency, it does not capture individual variations in network architecture. Recent studies have made progress in applying subject-specific connectivity to investigate AD pathology, demonstrating its potential for capturing individual variations in disease progression[33,73]. Future studies incorporating subject-specific connectivity could provide deeper insights into these mechanisms. Fourth, we assumed that the connectivity-dependent synaptic loss was similar to tau spreading, but a direct association between regional tau accumulation and synaptic loss propagation was not found in the current study, due to the limited sample size of patients with available tau PET and SV2A PET data.

In conclusion, the current study demonstrated that synaptic loss pattern is associated with brain connectivity in AD. Compactly connected regions are more vulnerable to synaptic loss along a functional architecture from synaptic loss epicenters. The concentration of plasm p-tau181 could enhance such connectivity-mediated synaptic loss. These findings support the hypothesis that synaptic loss patterns are partly shaped by brain network topology, potentially influenced by tau pathology. Our findings motivate future studies on the effect of tau spreading on network-constrained synaptic loss, and the synaptic mechanism underlying distinct phenotypes, given that synaptic loss is a major pathology driving cognitive impairments in AD. Moreover, the current study provides the potential for future research into individualized modeling of synaptic loss, which could help detect outcomes, measure treatment effectiveness, and predict disease progression in clinical trials.

Methods

Study design
This observational study aimed to test whether the synaptic loss pattern was shaped by brain connectome, and to model regional synaptic loss based on epicenter connectivity in AD. The participants were recruited since October 2020 from the memory clinic of Shanghai Jiao Tong University Affiliated Ruijin Hospital and surrounding communities. They were either self-referred in response to public advertisements or recruited during clinical visits when they or their family members reported subjective memory decline. Inclusion criteria required participants to be accompanied by a designated caregiver and to provide consent to complete questionnaire-based assessments and undergo PET and MRI imaging in accordance with the study protocol. Exclusion criteria included major psychiatric disorders, neurological or systemic conditions affecting cognition, a history of psychosis or intellectual disability, traumatic brain injury, contraindications to MRI, or inability to complete study procedures. Sex was determined based on self-reported biological sex. This study was approved by the Institutional Ethics Reviewing Board of Huashan Hospital, Fudan University (HS-KY-2020-916, HS-KY-2021-454). Ethical approval and written informed consent from all participants were obtained prior to the study by the investigators. All procedures were carried out in accordance with the Declaration of Helsinki.

Participants
The participants who had available data for baseline structural T1-weighted MRI, [18F]florbetapir (AV45) amyloid PET and [18F]SynVesT-1 SV2A-PET from the same study visit were included in this study. The amyloid status was characterized by visual rating of [18F]florbetapir PET images by two experienced readers[74]. The sample consisted of 54 CU Aβ- subjects and 91 Aβ+ patients, including 9 CU Aβ + , 28 MCI Aβ + , and 54 AD dementia. We additionally included one follow-up SV2A-PET scan from 18 Aβ+ subjects for longitudinal analyses. In order to obtain a normative network connectivity template, we additionally collected resting-state fMRI and multi-shell diffusion-weighted images (DWIs) data from 58 CU subjects with no evidence of abnormal amyloid-PET or tau-PET binding. The tau-PET negativity was determined through consensus visual interpretation of their 18F-MK6240 PET images by two independent readers, following the approach described previously[75]. Patients were diagnosed as dementia according to the 2018 National Institute on Aging and Alzheimer's Association (NIA-AA) diagnostic criteria[1]. MCI was defined using the actuarial neuropsychological method proposed by Jak and Bondi assessing three cognitive domains with six neuropsychological measures[76]: two indicators of episodic memory (long-delay free recall and recognition), measured with the Auditory Verbal Learning Test (AVLT); two indicators of language function, measured with the Animal Fluency Test (AFT) and the Boston Naming Test (BNT); and two indicators of executive function, measured by the Shape Trail Test (STT)-A and STT-B[77]; CU participants were defined as individuals who were excluded from a diagnosis of MCI or AD dementia with no impairment in any cognitive domain.

MRI and PET acquisition and preprocessing
SV2-PET scans were acquired on a 3 T PET/MR (uPMR 790, United Imaging Healthcare, Shanghai, China), in a 30-min time window starting 60 min after intravenous injection of ~185 MBq dose of 18F-SynVesT-1. AV45-PET was acquired in a 20-min frame 50 min after intravenous injection of 7.4 MBq/kg dose of 18F-florbetapir on a PET/CT scanner (Siemens Biograph 64 PET/CT). Acquired PET images were reconstructed by a filtered back projection algorithm with corrections for decay, normalization, dead time, photon attenuation, scatter, and random coincidences. A 3D Dixon sequence was acquired for attenuation correction and a T1 weighted MR scan was simultaneously acquired using the following parameters: repetition time=7200 ms, echo time=3.0 ms, flip angle=10°, acquisition matrix=256 × 329, in-plane resolution=1 mm × 1 mm, slice thickness = 1 mm, slices = 176. The resting-state fMRI data were obtained with a 3D echo-planar imaging (EPI) sequence with the parameters as follows: repetition time=800 ms, echo time=37.2 ms, flip angle = 52°, voxel size = 2 mm isotropic. We acquired 488 volumes with anterior-to-posterior (AP) phase encoding and 60 volumes with posterior-to-anterior (PA). The multi-shell diffusion-weighted images (DWIs) were acquired using a single shot spin-echo planar imaging sequence with the parameters as follows: repetition time = 6400 ms, echo time = 75 ms, voxel size = 1.5 mm isotropic, matrix size = 140 × 140, AP phase encoding was with b-values of 1500 s/mm2 (46 diffusion directions), 3000 s/mm2 (46 diffusion directions) and 7 b0 images interleaved. The PA phase encoding B0 images was acquired to correct magnetic susceptibility-induced phase encoding direction artifacts.

Structural T1-weighted MRI and PET images were preprocessed using SPM12 (Welcome Trust Centre for Neuroimaging, London, UK; https://www.fil.ion.ucl.ac.uk/spm). All structural MRI images were segmented into gray matter, white matter and cerebrospinal fluid (CSF). And spatially registered to Montreal Neurological Institute

(MNI) space with DARTEL algorithm. The PET images were co-registered to the native space T1-weighted MRI image and subsequently normalized to MNI space using spatial normalization parameters derived from corresponding T1-weighted images. Intensity normalization was performed using whole cerebellum derived from Automated Anatomical Labelling Atlas as the reference region to obtain standardized uptake value ratio (SUVR) maps for SV2A PET[78]. The cerebellar gray matter was used as the reference regions for AV45-PET. Spatially normalized grey matter maps were binarized at a threshold >0.3 to generate the grey matter masks for following analyses. Mean SV2A-PET values were subsequently extracted for each subject based on the 200 cortical-ROI in grey matter-masked Schaefer atlas. Global mean values of AV45-PET SUVR were also computed.

Preprocessing procedures for resting-state fMRI were applied as follows: (1) susceptibility induced-distortion correction with topup command in FSL, (2) removal of the first 10 volumes, (3) slicing timing and motion correction, (4) co-registration to native T1-weighted images, (5) regressing out mean signal from cerebrospinal fluid, white matter, and motion parameters, (6) detrending, band-pass filtering (0.01–0.08 Hz) and despiking, (7) spatial normalization to MNI space with the using spatial normalization parameters derived from corresponding T1-weighted images.

Preprocessing procedures for diffusion MRI images followed previously described pipeline[79]. The steps included: (1) denoising, (2) removal of Gibbs ringing artifacts, (3) correction for signal drift, (4) compensation for eddy current-induced distortions and head motion, (5) correction for susceptibility-induced distortions, and (6) B1 field inhomogeneity correction. White matter fiber orientation distribution (FOD) was estimated using the Multi-Shell Multi-Tissue Constrained Spherical Deconvolution (MSMT-CSD) model. To enhance the biological accuracy of tractography reconstruction, the tissue segmentation image derived from the T1-weighted image was transformed into diffusion MRI space. Multi-tissue informed log-domain intensity normalization was applied to all tissue types.

Construction of normative connectome templates

For our main analyses, a functional connectome template was generated using fMRI data from 58 Aβ- and tau-negative CU subjects in a ROI-wise manner based on the 200 ROIs of Schaefer functional MRI atlas[80]. The Schaefer functional atlas was masked with individual grey matter mask. The mean timeseries were computed for each ROI of the masked Schaefer functional atlas by averaging the BOLD signal across all voxels within the given ROI for each subject. Fisher-z transformed Pearson-moment correlations of the averaged timeseries between each pair of the ROIs were calculated to generate a functional connectivity matrix for each subject. The group-averaged ROI-wise functional connectivity template was obtained across the 58 subjects (Fig. 1C). Autocorrelations (i.e. the correlation of a ROI's timeseries with itself) were excluded for the following analyses. Negative functional connectivity values were also excluded when calculating the functional connectivity-weighted mean neighbor w score and mean functional connectivity to epicenter (for details see the following sections).

To assess whether synaptic loss is more closely associated with functional connectivity or structural connectivity, we also constructed a normative structural connectome template using diffusion MRI from the same 58 Aβ- and tau-negative CU subjects. Anatomically constrained tractography was performed with MRtrix3 using the iFOD2 algorithm to track 20 million streamlines (maximum length = 250 mm, minimum length = 5 mm, FOD amplitude = 0.05, curvature threshold = 45°) based on FOD-registered template. The registered T1-weighted tissue segmentation image ensured that streamlines terminated at the gray matter-white matter interface. To refine structural connection density estimation, we applied the SIFT2 algorithm. Inter-regional weighted number of streamlines were generated based on the Schaefer 200 atlas transformed into native space, resulting in a 200 ×

200 structural connectivity matrix per subject. A distance-dependent consensus approach was then used to derive a weighted group-level white matter connectome[81] and the weights of the group-level structural connectivity matrix were log-transformed.

Using the alternative 400-ROI parcellation of Schaefer atlas, the main results were replicated, yielding consistent findings (Supplementary Figs. 13–17).

Quantifying cross-sectional level and annual change rate of synaptic loss

To quantify regional synaptic loss, we computed ROI-wise W-scores of SV2A PET adopting previously described method to estimate the regional synaptic density loss in AD patients vs. controls[82]. In brief, we fitted a general linear model (GLM) for mean SV2A-PET SUVRs in the CU Aβ-group for each ROI with age, sex and cortical thickness as covariates. The intercept, regression coefficients of age, sex, cortical thickness, and the residuals of the control models were used to calculate the w-score following the formula:

$$W = \frac{(SUVR_{actual} - SUVR_{expected})}{SD_{residual}} \quad (1)$$

where $SUVR_{actual}$ is the observed SUVR, $SUVR_{expected}$ is the predicted SUVR from the control model, and $SD_{residual}$ is the standard deviation of residuals from the control model. In general, w-score reflects the standardized deviation of the SV2A-PET SUVR compared to CU Aβ-adjusted for covariates of age, sex and cortical thickness. The regional annual change rate of synaptic loss was further calculated as the difference of regional SV2A-PET w-score divided by the follow-up years.

Assessment of cross-sectional SV2A-PET w-score covariance

We then determined the baseline SV2A-PET w-score covariance by assessing the pairwise correlations of the SV2A-PET w-scores in gray matter-masked Schaefer atlas ROIs. In brief, we computed the ROI-to-ROI Spearman correlation coefficients of SV2A-PET w-scores across subjects due to the skewed distribution of SV2A-PET w-scores, resulting in a single 200 × 200 SV2A-PET w-score covariance matrix for CU Aβ- and Aβ+ subjects. The matrix subsequently underwent Fisher-z transformation.

Network spreading model

We assessed whether regional synaptic loss was constrained by the functional connectome by adapting a previously proposed network spreading approach[40]. This approach assumes that regional synaptic loss is associated with the collective contribution of synaptic loss in the neighbors and interregional functional connectivity. The model is defined as:

$$\hat{w}_i = \frac{1}{N_i} \sum_{j=1, j \neq i}^{N_i} w_j C_{ij} \quad (2)$$

Specifically, for a given ROI i, its SV2A-PET w score ($\hat{w}_i$) is modeled by the average of the SV2A-PET w score of its neighbor regions weighted by the interregional connectivity strength (C_{ij}), where w_j denotes the w score in neighbor region j. The model was assessed using the functional network at different levels of network sparsity (i.e., 100%, 75%, 50% and 25%), as well as the structural network. 25% indicates that 25% of the connections with the strongest functional connectivity strength were preserved in the network, while the remaining 75% of the connections were removed.

Baseline synaptic loss epicenter identification

We identified SV2A-PET epicenters at baseline following a previously proposed data-driven approach[40]. The epicenters were defined as the

regions showing substantial synaptic loss that were also strongly connected to regions with substantial synaptic loss (Fig. 4A). We calculated the mean rank of the baseline regional SV2A-PET w score and functional connectivity-weighted neighbor w-score as the epicenter likelihood. The epicenters were defined as those regions with significantly higher ranks than the distribution of null ranks derived from 1000 rotations of the SV2A-PET w-score map (one-sided $p_{spin} < 0.05$). We also adopted an alternative method of identifying the baseline epicenters as regions with the greatest synaptic loss by setting the threshold at 5%, 10%, 20% and 30%.

Null models

We compared the observed association against two kinds of null models to derive the significance[41]. The first null model (i.e. null spin) was to test the significance of the across-brain ROIs controlling for the spatial autocorrelation. Specifically, the empirical brain map was projected to the spherical surface and then randomly rotated. The regional values were reassigned to the nearest parcels. This procedure was repeated for 1000 times to obtain 1000 surrogate brain maps which preserved the spatial autocorrelation. The surrogate brain maps were generated by Neuromap toolbox[83]. The second null model (i.e. null rewired) was to generate 1000 null connectomes with preserved degree- and weight-distribution of the empirical connectivity connectome. The surrogate networks were generated by Brain Connectivity Toolbox. *P*-value was determined by comparing the true statistic with the null distribution of statistics obtained by repeating the analyses with 1000 spin maps or rewired networks.

Plasma phosphorylated tau 181

Plasma samples were collected prior to PET tracer injection, stored at −80°C, and later analyzed for p-tau181 using single molecular arrays (Simoa) HD-1 platform from Quanterix[84] (Billerica, MA, USA) and the p-tau-181 Advantage V2 kit (Lot 502923). All assays were performed blinded to clinical data, and results were expressed in pg/mL.

Immunohistochemistry and immunofluorescence staining of postmortem human brain tissue

Postmortem brain tissues from 5 pathologically confirmed AD patients and 4 normal controls (see Supplementary Table 6 for details) were obtained from the Netherlands Brain Bank (NBB). All materials were collected from donors or from whom written informed consent was obtained for a brain autopsy, and the use of the materials and clinical information for research purposes were obtained by the NBB. All procedures involving human postmortem tissue were approved by the regional human ethics committee and the Medical Ethics Committee of the VU University Medical Center (2009/148), in accordance with the Declaration of Helsinki. Paraffin-embedded sections of the entorhinal cortex were cut into 3μm slices using a Leica microtome (Leica Microsystems, Germany). Antigen retrieval of the paraffin-embedded fixed human brain tissue sections was performed with citrate buffer. First, the sections were heated in buffer for seven minutes at 700 W, followed by 20 minutes at 280 W. Last, the sections were kept at room temperature without a cover for 20 minutes. After being blocked in 5% donkey serum in 1% Triton-PBS, the sections were incubated at 4 °C with mild shaking with primary antibodies SV2A (rabbit monoclonal, clone EPR23500-32, Abcam, cat. no. ab254351, Lot no. 1041815-5, 1:1000), p-tau (mouse monoclonal, clone AT8, Invitrogen, cat. no. MN1020, Lot no. VL3113305, dilution 1:1000), and β-amyloid (mouse monoclonal, clone 4G8, BioLegend, cat. no. 800701, Lot. No B246022, 1:4000). For immunofluorescence staining (AT8) on the following day, sections were washed twice with PBS for 20 minutes and incubated with appropriate secondary antibodies for 2 hours at room temperature. Nuclear counterstaining was performed with 4′,6-diamidino-2-phenylindole (DAPI) for 15 minutes, followed by two PBS washes (10 minutes each). For immunochemical staining (4G8, SV2A),

the sections were then rinsed three times for 10 min each in 0.1 M PBS before being incubated with a biotinylated anti-mouse secondary antibody (suspended in 0.1 M PBS with 0.5% v/v Triton-X) for 2 h. The sections were then incubated with an avidin-biotin complex−horseradish peroxidase for 1 h at room temperature. The sections were developed with 0.025% 3,3′-diaminobenzidine and 0.05% H2O2 in triphosphate-buffered saline (TBS, pH 7.4) for 3 min. After being mounted on slides, the sections were dehydrated by an ascending alcohol series of 70%, 90%, and 100% (twice each) and Roticlear® for 2 min. Coverslips were finally mounted with Rotimount® mounting medium. The primary and secondary antibodies used are listed in Supplementary Table 7. The brain sections were imaged at ×20 magnification using an Axio Observer Z1 slide scanner (Zeiss, Germany) using the same acquisition settings. Images were analyzed using Qupath and ImageJ (National Institutes of Health).

Statistics

Demographics were compared between diagnostic groups using analyses of variance (ANOVAs) for continuous variables and chi-square tests for categorical variables.

To test our first hypothesis, i.e., that stronger brain connectivity between two regions is associated with shared levels of cross-sectional synaptic loss between the given regions, we performed linear regression of vectorized covariance in the baseline SV2A PET w-score matrix against the normative connectivity matrix. To explore whether the association between the functional connectome and covariance in baseline SV2A-PET w-score was stronger in Aβ+ participants than in CU Aβ− participants, we determined resampled covariances in the SV2A-PET w score by 1000 bootstrapping iterations, yielding 1000 β values from the linear regressions of bootstrapped covariance and functional connectivity in the CU Aβ− group and pooled Aβ+ group, respectively. Two-sample t tests were applied to compare the distributions of bootstrapped β values between the two groups. Furthermore, to assess whether functional or structural connectivity better explains the covariance in SV2A-PET w-score, we performed paired t tests to compare the distribution of 1000 bootstrapped β values from functional and structural connectivity matrices in Aβ+ group. To avoid the effect of geometric proximity, the inter-regional Euclidean distance was additionally controlled for in aforementioned analyses.

Next, we tested our second hypothesis that the degree of cross-sectional synaptic loss is associated with the synaptic loss in connected regions. To this end, we calculated for each ROI the connectivity-weighted mean neighbor w-score according to the formula described in the Network spreading model section separately using the functional network at the network sparsity of 25%-100% and structural network. A linear regression model was then employed to assess the association between the baseline SV2A-PET w-score and the connectivity-weighted mean neighbor w-score in pooled Aβ+ subjects. The significance of associations was determined by comparing the observed model with two null models. The association was evaluated for each Aβ+ subject. The distributions of subject-level regression-derived β values were tested against zero using one-sample t-tests. We further included the mean Euclidean distance to each ROI as an additional covariate. To demonstrate that AD exacerbates the network-based synaptic loss, we estimated the subject-level association among CU Aβ- subjects and compared the distribution of subject-level β values between CU Aβ- and Aβ+ subjects with ANCOVA with age, sex, education years and clinical diagnosis as the covariates. For exploratory purpose, the group difference of APOE4 carriage in Aβ+ subjects was additionally tested on the subject-level regression-derived β values, adjusting for age, sex, and clinical diagnosis.

We further assessed whether the cross-sectional synaptic loss levels can be modelled as a function of the connectivity pattern to epicenter. The mean functional connectivity to baseline epicenter for an ROI was calculated as its averaged functional connectivity to the

epicenter ROIs. A linear regression was applied to model group-average SV2A-PET w score based on the functional connectivity to group-level SV2A w score epicenter in Aβ+ subjects. Subsequently, we extended our analyses to the subject level by adopting a previously proposed approach[42,58]. Briefly, for each participant, subject-specific epicenter was identified, and cortical ROIs were grouped into 4 quantiles according to their mean connectivity to subject-specific epicenter ROIs (i.e., Q1-Q4 ROIs). The mean SV2A-PET w scores across the ROIs of each quartile were subsequently computed for each participant. We applied linear mixed effect regression to test the associations between the epicenter connectivity quartiles and the mean SV2A-PET w scores of the Q1-Q4 ROIs, accounting for the fixed effects of age, sex, clinical diagnosis, and education years, as well as random intercepts. Euclidean distance to epicenter was additionally included as a covariate at both group- and subject-level analyses. Subject-level linear mixed effect regression models were also repeated with APOE4 status as an additional covariate to evaluate effect of APOE4 status in Aβ+ subjects. To further test the robustness of the subject-level modeling of SV2A-PET w score with epicenter connectivity, we subsequently derived the subject-level association (i.e., β-values) between functional connectivity to subject-specific epicenter and individual SV2A-PET w score by linear regression models. Then we compared the actual β-value with the null distribution of 1000 β-values from null spin and null rewired models. The group difference in subject-level epicenter connectivity-based synaptic loss (i.e. β-values) was compared between CU Aβ- and Aβ+ subjects using linear regression adjusting the covariates of age, sex, and education years, as well as APOE4 carriers and noncarriers.

Hierarchical clustering was performed to stratify Aβ+ participants into several spatially distinct subtypes to capture the heterogeneity in synaptic loss pattern in AD. The optimal number of clusters was assessed using the R package NbClust, by which the clustering scheme that satisfies most of the 30 metrics is reported. For each subtype, we defined the subtype-specific epicenter and tested the association between regional synaptic loss and epicenter connectivity at group level. Subject-level analyses were also applied as described above across the subjects belonging to each subtype. To further validate the results for severity-dependent stage of synaptic loss propagation, we iteratively selected a subset of Aβ+ subjects for each predefined subtype using the sliding window method, in which we moved a window for 8 ordered subjects according to the global mean SV2A-PET w score, and replicated the epicenter connectivity-based modeling of SV2A w score for each window. The epicenter in each sliding window was constantly defined as the subtype-specific epicenter across all participants in corresponding subtype.

Next, we tested whether the functional connectivity to baseline epicenter of synaptic loss is associated with longitudinal change of synaptic loss (i.e., the annual change rate of SV2A-PET w-score) in connected brain regions in a subset of 18 Aβ+ participants. We applied a linear regression model for group-level analysis, controlling for the baseline regional SV2A-PET w-score. Due to the limited sample size of longitudinal data, we repeated the analyses on 1000 bootstrapping samples and tested the significance by one sample t test. At a subject level, the association between functional connectivity to subject-specific epicenter and regional SV2A-PET w-score change rate was estimated by the β-value derived from the linear regression model controlling for baseline regional SV2A-PET w-score. The β-values were tested against zero using one-sample t test. Euclidean distance was additionally included as a covariate to test the consistency.

Lastly, we investigated the effect of p-tau and Aβ on the connectivity-mediated synaptic loss. Among 88 subjects with plasma p-tau181 data available, we separately examined the interaction effect of plasma p-tau181 and global AV45-PET SUVR with epicenter connectivity to connected 4 quartiles (i.e., Q1-Q4) on SV2A-PET w-score

using linear mixed effect model, accounting for the fixed effects of age, sex, and education years, as well as random intercepts. We subsequently assessed the direct association between subject-level epicenter connectivity-based SV2A-PET w score (i.e., regression-derived β-values) and plasma p-tau181 as well as global AV45-PET SUVR using the linear regression controlling for age, sex and education years. The analyses were repeated for pooled participants, including both CU Aβ- and Aβ+ individuals, as well as for Aβ+ participants alone. For the models with plasma p-tau181, we additionally controlled for global AV45-PET SUVR. Furthermore, a mediation analysis was performed to assess whether the plasma p-tau181 levels mediate the relationship between the global AV45-PET SUVR and connectivity-mediated SV2A w-score, using the R package mediation (Version 4.5.0). The statistical significance of the mediation effect was determined by 1000 bootstrapping iterations. APOE4 carriage was additionally included as an additional covariate to test the consistency of the results. The difference of AT8 and SV2A levels in the post-mortem entorhinal cortex tissue was tested by Mann-Whitney test. The relation between AT8 and SV2A was tested using Spearman correlation.

For exploratory purposes, we repeated the main analyses, only including the Aβ + MCI and dementia participants given the low levels of synaptic density alteration in Aβ + CU (Fig. 1). The replicated results were consistent with the main findings (Supplementary Figs. 18–20). All effects were considered significant at an alpha threshold of 0.05. All the statistical analyses were performed in R (version 4.3.1). The brain surface maps were rendered using the connectome workbench.

Reporting summary
Further information on research design is available in the Nature Portfolio Reporting Summary linked to this article.

Data availability
The processed neuroimaging data and other data used in this study have been deposited on GitHub (https://github.com/yluan-seu/SV2A_propagation)[85]. Data and intermediate results for reproducing our findings are provided in the Source Date file. The raw neuroimage data are not publicly available due to privacy concerns and ethical restrictions. Data access can be granted upon request to the corresponding authors, subject to institutional review and the signing of a data use agreement that outlines the terms of access, use, storage and authorship requirements. Requests will be reviewed within approximately 2–4 weeks. Source data are provided with this paper.

Code availability
Software used to preprocess the neuroimaging data in the study included SPM12 (https://www.fil.ion.ucl.ac.uk/spm), FSL 6.0.1 (https://fsl.fmrib.ox.ac.uk/fsl/fslwiki), AFNI, ANTs 2.5.2 (https://github.com/ANTsX/ANTs), and Diffusion Image Operator (iDIO) pipeline (https://github.com/iDIO4dMRI/iDIO). All analyses were performed using R statistical software 4.4.2. Example R code of the main analyses in this study can be found on GitHub (https://github.com/yluan-seu/SV2A_propagation)[85].

References
1. Jack, C. R. Jr. et al. NIA-AA research framework: toward a biological definition of Alzheimer's disease. *Alzheimer's Dement.* **14**, 535–562 (2018).
2. Terry, R. D. et al. Physical basis of cognitive alterations in Alzheimer's disease: synapse loss is the major correlate of cognitive impairment. *Ann. Neurol.: Off. J. Am. Neurological Assoc. Child Neurol. Soc.* **30**, 572–580 (1991).
3. Chen, M.-K. et al. Assessing synaptic density in Alzheimer disease with synaptic vesicle glycoprotein 2A positron emission tomographic imaging. *JAMA Neurol.* **75**, 1215–1224 (2018).

4. Naganawa, M. et al. First-in-human evaluation of (18)f-synvest-1, a radioligand for pet imaging of synaptic vesicle glycoprotein 2A. *J. Nucl. Med* **62**, 561–567 (2021).

5. Finnema, S. J. et al. Imaging synaptic density in the living human brain. *Sci. Transl. Med* **8**, 348ra396 (2016).

6. Paus, T., Pesaresi, M. & French, L. White matter as a transport system. *Neuroscience* **276**, 117–125 (2014).

7. Park, H. J. & Friston, K. Structural and functional brain networks: from connections to cognition. *Science* **342**, 1238411 (2013).

8. Fornito, A., Zalesky, A. & Breakspear, M. The connectomics of brain disorders. *Nat. Rev. Neurosci*. **16**, 159–172 (2015).

9. Arnatkeviciute, A., Fulcher, B. D., Bellgrove, M. A. & Fornito, A. Where the genome meets the connectome: Understanding how genes shape human brain connectivity. *Neuroimage* **244**, 118570 (2021).

10. Richiardi, J. et al. BRAIN NETWORKS. Correlated gene expression supports synchronous activity in brain networks. *Science* **348**, 1241–1244 (2015).

11. Spreng, R. N. & Turner, G. R. Structural covariance of the default network in healthy and pathological aging. *J. Neurosci*. **33**, 15226–15234 (2013).

12. Alexander-Bloch, A., Raznahan, A., Bullmore, E. & Giedd, J. The convergence of maturational change and structural covariance in human cortical networks. *J. Neurosci*. **33**, 2889–2899 (2013).

13. Walsh, D. M. & Selkoe, D. J. A critical appraisal of the pathogenic protein spread hypothesis of neurodegeneration. *Nat. Rev. Neurosci*. **17**, 251–260 (2016).

14. Zhu, F. et al. Architecture of the mouse brain synaptome. *Neuron* **99**, 781–799 e710 (2018).

15. Klug, S. et al. Synaptic signaling modeled by functional connectivity predicts metabolic demands of the human brain. *NeuroImage* **295**, 120658 (2024).

16. Kuchibhotla, K. V. et al. Aβ plaques lead to aberrant regulation of calcium homeostasis in vivo resulting in structural and functional disruption of neuronal networks. *Neuron* **59**, 214–225 (2008).

17. Edwards, F. A. A unifying hypothesis for Alzheimer's disease: from plaques to neurodegeneration. *Trends Neurosci*. **42**, 310–322 (2019).

18. John, A. & Reddy, P. H. Synaptic basis of Alzheimer's disease: Focus on synaptic amyloid beta, P-tau and mitochondria. *Ageing Res. Rev*. **65**, 101208 (2021).

19. Tzioras, M., McGeachan, R. I., Durrant, C. S. & Spires-Jones, T. L. Synaptic degeneration in Alzheimer disease. *Nat. Rev. Neurol*. **19**, 19–38 (2023).

20. Hoover, B. R. et al. Tau mislocalization to dendritic spines mediates synaptic dysfunction independently of neurodegeneration. *Neuron* **68**, 1067–1081 (2010).

21. Ittner, L. M. et al. Dendritic function of tau mediates amyloid-β toxicity in Alzheimer's disease mouse models. *Cell* **142**, 387–397 (2010).

22. O'Dell, R. S. et al. Association of Aβ deposition and regional synaptic density in early Alzheimer's disease: a PET imaging study with [11 C] UCB. *J. Alzheimer's Res. Ther*. **13**, 1–12 (2021).

23. Vanhaute, H. et al. In vivo synaptic density loss is related to tau deposition in amnestic mild cognitive impairment. *Neurology* **95**, e545–e553 (2020).

24. Coomans, E. M. et al. In vivo tau pathology is associated with synaptic loss and altered synaptic function. *Alzheimer's Res. Ther*. **13**, 1–13 (2021).

25. Mecca, A. P. et al. Association of entorhinal cortical tau deposition and hippocampal synaptic density in older individuals with normal cognition and early Alzheimer's disease. *Neurobiol. aging* **111**, 44–53 (2022).

26. Koffie, R. M. et al. Oligomeric amyloid β associates with postsynaptic densities and correlates with excitatory synapse loss near senile plaques. *Proc. Natl Acad. Sci*. **106**, 4012–4017 (2009).

27. Pereira, J. B. et al. Untangling the association of amyloid-beta and tau with synaptic and axonal loss in Alzheimer's disease. *Brain* **144**, 310–324 (2021).

28. Hong, S. et al. Complement and microglia mediate early synapse loss in Alzheimer mouse models. *Science* **352**, 712–716 (2016).

29. Polydoro, M. et al. Soluble pathological tau in the entorhinal cortex leads to presynaptic deficits in an early Alzheimer's disease model. *Acta neuropathologica* **127**, 257–270 (2014).

30. Watamura, N. et al. In vivo hyperphosphorylation of tau is associated with synaptic loss and behavioral abnormalities in the absence of tau seeds. *Nat. Neurosci*. **28**, 293–307 (2025).

31. Vogel, J. W. et al. Connectome-based modelling of neurodegenerative diseases: towards precision medicine and mechanistic insight. *Nat. Rev. Neurosci*. **24**, 620–639 (2023).

32. Franzmeier, N. et al. Functional brain architecture is associated with the rate of tau accumulation in Alzheimer's disease. *Nat. Commun*. **11**, 347 (2020).

33. Ottoy, J. et al. Tau follows principal axes of functional and structural brain organization in Alzheimer's disease. *Nat. Commun*. **15**, 5031 (2024).

34. Vogel, J. W. et al. Spread of pathological tau proteins through communicating neurons in human Alzheimer's disease. *Nat. Commun*. **11**, 2612 (2020).

35. Iturria-Medina, Y., Sotero, R. C., Toussaint, P. J., Evans, A. C. & Alzheimer's Disease Neuroimaging, I. Epidemic spreading model to characterize misfolded proteins propagation in aging and associated neurodegenerative disorders. *PLoS Comput Biol*. **10**, e1003956 (2014).

36. Raj, A. et al. Network diffusion model of progression predicts longitudinal patterns of atrophy and metabolism in Alzheimer's disease. *Cell Rep*. **10**, 359–369 (2015).

37. Zhou, J., Gennatas, E. D., Kramer, J. H., Miller, B. L. & Seeley, W. W. Predicting regional neurodegeneration from the healthy brain functional connectome. *Neuron* **73**, 1216–1227 (2012).

38. Perry, D. C. et al. Clinicopathological correlations in behavioural variant frontotemporal dementia. *Brain* **140**, 3329–3345 (2017).

39. Tetreault, A. M. et al. Network localization of clinical, cognitive, and neuropsychiatric symptoms in Alzheimer's disease. *Brain* **143**, 1249–1260 (2020).

40. Shafiei, G. et al. Spatial patterning of tissue volume loss in schizophrenia reflects brain network architecture. *Biol. Psychiatry* **87**, 727–735 (2020).

41. Chopra, S. et al. Network-based spreading of gray matter changes across different stages of psychosis. *JAMA Psychiatry* **80**, 1246–1257 (2023).

42. Franzmeier, N. et al. Tau deposition patterns are associated with functional connectivity in primary tauopathies. *Nat. Commun*. **13**, 1362 (2022).

43. Steward, A. et al. Apoe4 and connectivity-mediated spreading of tau pathology at lower amyloid levels. *JAMA Neurol*. **80**, 1295–1306 (2023).

44. Braak, H. & Braak, E. Neuropathological staging of Alzheimer-related changes. *Acta Neuropathol*. **82**, 239–259 (1991).

45. Fang, X. T. et al. Linking resting-state network fluctuations with systems of coherent synaptic density: A multimodal fMRI and (11)C-UCB-J PET study. *Front Hum. Neurosci*. **17**, 1124254 (2023).

46. Fang, X. T. et al. Identifying brain networks in synaptic density PET ((11)C-UCB-J) with independent component analysis. *Neuroimage* **237**, 118167 (2021).

47. Di, X., Biswal, B. B. & Alzheimer's Disease Neuroimaging Initiative Metabolic brain covariant networks as revealed by FDG-PET with reference to resting-state fMRI networks. *Brain connectivity* **2**, 275–283 (2012).

48. Richiardi, J. et al. Correlated gene expression supports synchronous activity in brain networks. *Science* **348**, 1241–1244 (2015).

49. Vertes, P.E. et al. Gene transcription profiles associated with inter-modular hubs and connection distance in human functional magnetic resonance imaging networks. *Philos. Trans. R. Soc. Lond. Biol. Sci.* **371**, https://doi.org/10.1098/rstb.2015.0362 (2016).

50. Hansen, J. Y. et al. Mapping neurotransmitter systems to the structural and functional organization of the human neocortex. *Nat. Neurosci.* **25**, 1569–1581 (2022).

51. Grothe, M. J. et al. Molecular properties underlying regional vulnerability to Alzheimer's disease pathology. *Brain* **141**, 2755–2771 (2018).

52. Sepulcre, J. et al. Neurogenetic contributions to amyloid beta and tau spreading in the human cortex. *Nat. Med* **24**, 1910–1918 (2018).

53. Markham, J. A. & Greenough, W. T. Experience-driven brain plasticity: beyond the synapse. *Neuron glia Biol.* **1**, 351–363 (2004).

54. O'Rourke, N. A., Weiler, N. C., Micheva, K. D. & Smith, S. J. Deep molecular diversity of mammalian synapses: why it matters and how to measure it. *Nat. Rev. Neurosci.* **13**, 365–379 (2012).

55. Alonso-Nanclares, L., Gonzalez-Soriano, J., Rodriguez, J. & DeFelipe, J. Gender differences in human cortical synaptic density. *Proc. Natl Acad. Sci.* **105**, 14615–14619 (2008).

56. Cizeron, M. et al. A brainwide atlas of synapses across the mouse life span. *Science* **369**, 270–275 (2020).

57. Hoenig, M. C. et al. Networks of tau distribution in Alzheimer's disease. *Brain* **141**, 568–581 (2018).

58. Franzmeier, N. et al. Patient-centered connectivity-based prediction of tau pathology spread in Alzheimer's disease. *Sci. Adv.* **6**, eabd1327 (2020).

59. Zhou, L. et al. Tau association with synaptic vesicles causes presynaptic dysfunction. *Nat. Commun.* **8**, 15295 (2017).

60. McInnes, J. et al. Synaptogyrin-3 Mediates Presynaptic Dysfunction Induced by Tau. *Neuron* **97**, 823–835 e828 (2018).

61. Largo-Barrientos, P. et al. Lowering Synaptogyrin-3 expression rescues Tau-induced memory defects and synaptic loss in the presence of microglial activation. *Neuron* **109**, 767–777 e765 (2021).

62. Callahan, L. M., Vaules, W. A. & Coleman, P. D. Quantitative decrease in synaptophysin message expression and increase in cathepsin D message expression in Alzheimer disease neurons containing neurofibrillary tangles. *J. Neuropathol. Exp. Neurol.* **58**, 275–287 (1999).

63. Vanderlinden, G. et al. Longitudinal synaptic loss versus tau Braak staging in amnestic mild cognitive impairment. *Alzheimers Dement* **21**, e14412 (2025).

64. Holland, N. et al. Molecular pathology and synaptic loss in primary tauopathies: an 18F-AV-1451 and 11C-UCB-J PET study. *Brain* **145**, 340–348 (2022).

65. Taddei, R. N. & K, E. D. Synapse vulnerability and resilience underlying Alzheimer's disease. *EBioMedicine* **112**, 105557 (2025).

66. Mecca, A. P. et al. In vivo measurement of widespread synaptic loss in Alzheimer's disease with SV2A PET. *Alzheimer's Dement.* **16**, 974–982 (2020).

67. Saroja, S. R., Sharma, A., Hof, P. R. & Pereira, A. C. Differential expression of tau species and the association with cognitive decline and synaptic loss in Alzheimer's disease. *Alzheimer's Dement.* **18**, 1602–1615 (2022).

68. Ohrfelt, A. et al. Association of CSF GAP-43 With the Rate of Cognitive Decline and Progression to Dementia in Amyloid-Positive Individuals. *Neurology* **100**, e275–e285 (2023).

69. Roberson, E. D. et al. Reducing endogenous tau ameliorates amyloid β-induced deficits in an Alzheimer's disease mouse model. *Science* **316**, 750–754 (2007).

70. Crimins, J. L., Pooler, A., Polydoro, M., Luebke, J. I. & Spires-Jones, T. L. The intersection of amyloid beta and tau in glutamatergic synaptic dysfunction and collapse in Alzheimer's disease. *Ageing Res. Rev.* **12**, 757–763 (2013).

71. Lan, G. et al. Association of APOE-ε4 and GAP-43-related pre-synaptic loss with β-amyloid, tau, neurodegeneration, and cognitive decline. *Neurobiol. Aging* **132**, 209–219 (2023).

72. Kumar, A., Scarpa, M. & Nordberg, A. Tracing synaptic loss in Alzheimer's brain with SV2A PET-tracer UCB-J. *Alzheimers Dement* **20**, 2589–2605 (2024).

73. Roemer-Cassiano, S. N. et al. Amyloid-associated hyperconnectivity drives tau spread across connected brain regions in Alzheimer's disease. *Sci. Transl. Med.* **17**, eadp2564 (2025).

74. Johnson, K. A. et al. Appropriate use criteria for amyloid PET: a report of the Amyloid Imaging Task Force, the Society of Nuclear Medicine and Molecular Imaging, and the Alzheimer's Association. *Alzheimers Dement* **9**, e-1–16 (2013).

75. Shuping, J. L. et al. Development, initial validation, and application of a visual read method for [18F] MK-6240 tau PET. *Alzheimer's Dement.: Transl. Res. Clin. Interventions* **9**, e12372 (2023).

76. Bondi, M. W. et al. Neuropsychological criteria for mild cognitive impairment improves diagnostic precision, biomarker associations, and progression rates. *J. Alzheimers Dis.* **42**, 275–289 (2014).

77. Huang, L., Chen, K., Liu, Z. & Guo, Q. A Conceptual Framework for Research on Cognitive Impairment with no Dementia in Memory Clinic. *Curr. Alzheimer Res* **17**, 517–525 (2020).

78. Naganawa, M. et al. Noninvasive quantification of [(18)F]SynVesT-1 binding using simplified reference tissue model 2. *Eur. J. Nucl. Med Mol. Imaging* **52**, 113–121 (2024).

79. Hsu, C. H. et al. Integrated diffusion image operator (iDIO): A pipeline for automated configuration and processing of diffusion MRI data. *Hum. Brain Mapp.* **44**, 2669–2683 (2023).

80. Schaefer, A. et al. Local-Global Parcellation of the Human Cerebral Cortex from Intrinsic Functional Connectivity MRI. *Cereb. Cortex* **28**, 3095–3114 (2018).

81. Betzel, R. F., Griffa, A., Hagmann, P. & Mišić, B. Distance-dependent consensus thresholds for generating group-representative structural brain networks. *Netw. Neurosci.* **3**, 475–496 (2019).

82. Chung, J. et al. Normalization of cortical thickness measurements across different T1 magnetic resonance imaging protocols by novel W-Score standardization. *Neuroimage* **159**, 224–235 (2017).

83. Markello, R. D. et al. neuromaps: structural and functional interpretation of brain maps. *Nat. Methods* **19**, 1472–1479 (2022).

84. Wilson, D. H. et al. The Simoa HD-1 Analyzer: A Novel Fully Automated Digital Immunoassay Analyzer with Single-Molecule Sensitivity and Multiplexing. *J. Lab Autom.* **21**, 533–547 (2016).

85. Luan, Y. yluan-seu/SV2A_propagation: SV2A_connectome (v1.0.0). Zenodo. https://doi.org/10.5281/zenodo.15609808 (2025).

Author contributions

Conceptualization and study design: F.X., Y.L., Q.H. Acquisition and analyses of data: Y.L., W.W., J.W., Y.W. Methodology: Y.L., A.S., S.N.R., N.F., M.E. Interpretation of results: Y.L., W.W., A.S., S.N.R., R.N. Brain tissue staining: J.N. Funding acquisition: F.X., Y.L., Q.H., Y.G. Project administration and supervision: F.X. Writing – original draft: Y.L., W.W., F.X. Writing – review & editing: Y.L., W.W., A.S., S.N. R., Y.G., B.L., M.E., M.S., R.N., N.F., F.X.

Competing interests

The authors declare no competing interests.

Additional information